Chapter 13. Microwave Study Programs of Air–Ice–Ocean Interactive Processes in the Seasonal Ice Zone of the Greenland and Barents Seas

OLA M. JOHANNESSEN

Nansen Environmental and Remote Sensing Center, Solheimsvik, Bergen N-5037, Norway

WILLIAM J. CAMPBELL

U.S. Geological Survey, University of Puget Sound, Tacoma, Washington 98416

ROBERT SHUCHMAN

Environmental Research Institute of Michigan, P. O. Box 8618, Ann Arbor, Michigan 48107

STEIN SANDVEN

Nansen Environmental and Remote Sensing Center, Solheimsvik, Bergen N-5037, Norway

PER GLOERSEN

Goddard Space Flight Center, Greenbelt, Maryland 20771

JOHNNY A. JOHANNESSEN

Nansen Environmental and Remote Sensing Center, Solheimsvik, Bergen N-5037, Norway

EDWARD G. JOSBERGER

U.S. Geological Survey, University of Puget Sound, Tacoma, Washington 98416

PETER M. HAUGAN

Nansen Environmental and Remote Sensing Center, Solheimsvik, Bergen N-5037, Norway

13.1 INTRODUCTION

Following the International Geophysical Year (1957 through 1958), a series of large field experiments was performed, culminating in the Arctic Ice Dynamics Joint Experiment, AIDJEX (1972 through 1976). These experiments considerably aided our understanding of the growth, motion, and decay of sea ice in the interior of the Arctic Ocean [Untersteiner, 1986; Pritchard, 1980; Campbell et al., 1978; Gloersen et al., 1978]. With these experiments concluded and coupled nonlinear sea ice dynamic–thermodynamic models in hand [Hibler, 1979; Coon, 1980], attention shifted to the problem of understanding the processes that occur near the open ocean boundaries of polar sea ice covers. The seasonal ice zone (SIZ) is the crucial region in which the polar atmosphere, sea ice covers, and oceans interact with the bordering atmosphere and oceans. The air–ice–ocean processes and exchanges that take place there determine the advance and retreat of the sea ice and profoundly influence the global climate. These processes also exert a significant effect on marine productivity, commercial fisheries, petroleum exploration and production, and naval operations [Johannessen et al., 1984a; Wadhams, 1986; Sandven and Johannessen, 1990].

Remote sensing is an essential tool in the study of the SIZ. Some examples of different remote sensing data used in the study of SIZ processes are shown in Figure 13-1. Figure 13-1(a) shows the total ice concentration of the Northern Hemisphere for February 1989, as observed by the Special Sensor Microwave Imager (SSM/I). These observations provide daily information on ice edge position and concentration of first-year and multiyear ice with a resolution of 30 km. They show many regional features that repeatedly occur in the SIZ. For example, an historically important feature, the Odden (a region of rapid ice growth and advance that generally occurs every winter), can be seen projecting northeastward into the central Greenland Sea. The long time series of similar images acquired from the Nimbus 5 Electrically Scanning Microwave Radiometer (ESMR) from 1973 to 1976 [Zwally et al., 1983; Parkinson et al., 1987], the Nimbus 7 Scanning Multichannel Microwave Radiometer (SMMR) from 1978 to 1987, and the SSM/I from 1987 to the present provides a
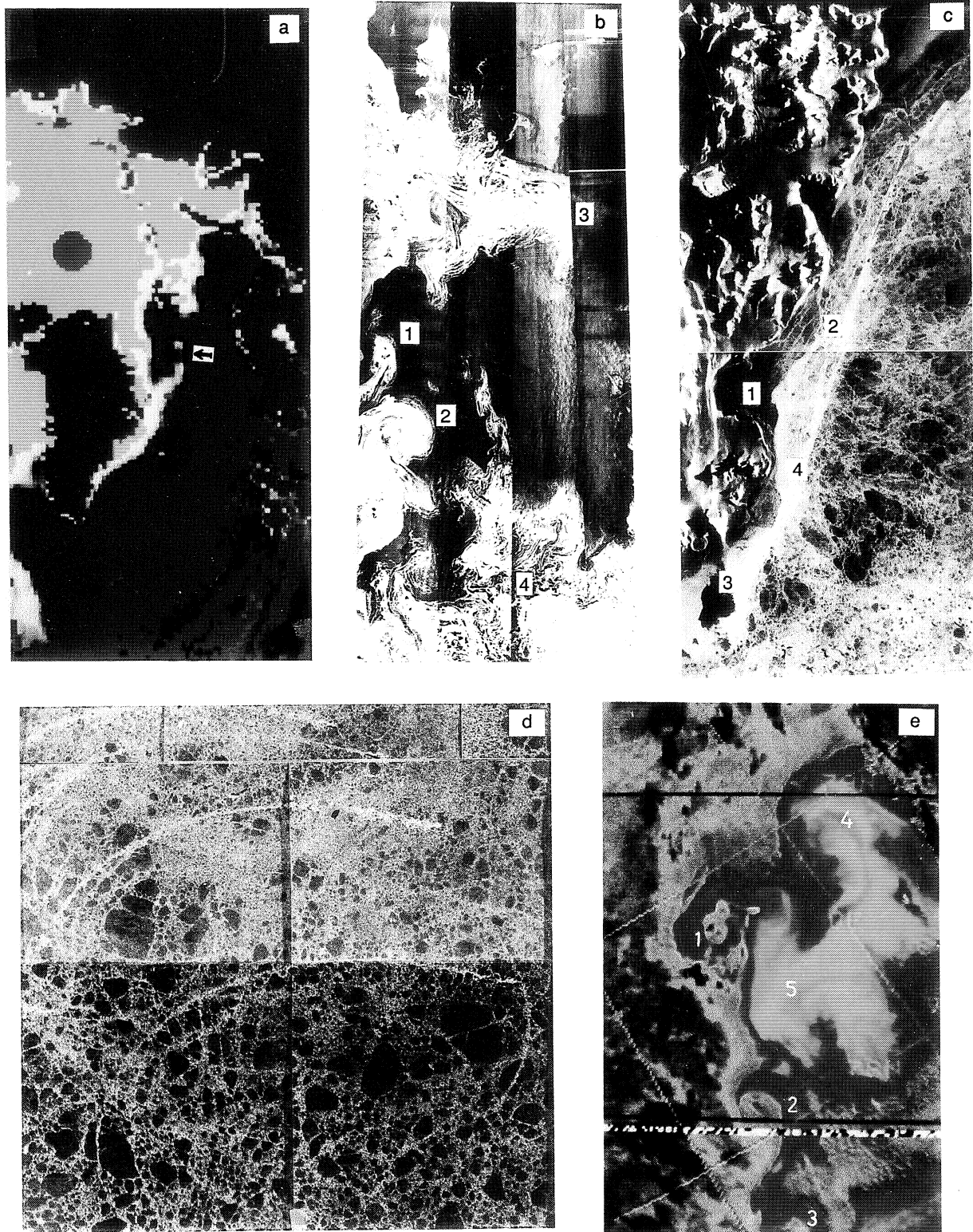
Fig. 13-1. (a) SSM/I image of ice concentration in the Northern Hemisphere on February 18, 1989. Yellow indicates concentration above 90% and dark blue is open water. The arrow shows the location of the ice tongue Odden. (b) Airborne SAR image from the Greenland Sea obtained on March 28 and 29, 1987, showing a (1) vortex-pair, (2) anticyclonic ice-ocean eddy, (3) family of eddies over the Molloy Deep, and (4) newly formed ice. (c) Airborne SAR image from February 23, 1989, of the ice off the east coast of Svalbard, showing (1) land-fast ice, (2) shear zones, (3) polynyas, and (4) ridges. (d) SAR image of the Barents Sea ice cover showing the curved tracks of grounded icebergs. The image was obtained on March 23, 1988. (e) NOAA AVHRR image of ice edge eddies (1 through 5) in the Greenland Sea on July 4, 1984.

unique 16-year record that is extremely important for SIZ and global change studies [Gloersen and Campbell 1991a, b; Gloersen et al., 1992].

Of all the passive and active microwave sensors, synthetic aperture radars (SAR's) provide the highest resolution ice information. Sequential SAR images, with a resolution as fine as 5 m, provide quantitative information about the growth, motion, and decay of ice edge eddies and other mesoscale features [Johannessen et al., 1983a, 1987; Shuchman et al., 1987; Campbell et al., 1987; Johannessen, 1987] in addition to ice concentration, type, and kinematics [Burns et al., 1987]. The SAR image from the Greenland Sea acquired during MIZEX'87 on March 28 and 29, Figure 13-1(b), reveals how extremely complex the morphology of the marginal ice zone can be and how powerful a tool SAR can be for the study of ice edge structure. On the day this image was acquired, the surface wind speed was low and the air was cold (–10°C); therefore, the ice mirrored the mesoscale ocean circulation and freezing processes. In this image, bright signatures derive from various types of ice, while the dark signatures are from ice-free water. In the western central Greenland Sea, Figure 13-1(b) shows a narrow jet shooting out from the ice edge and ending in a vortex-pair with a scale of 10 to 20 km [MIZEX Group, 1989]. Slightly south of this vortex-pair is a clearly defined anticyclonic ice-ocean eddy with a diameter of about 30 km. In the northern Greenland Sea in this image, a family of eddies are centered over the 5500-m depression known as the Molloy Deep, shown in the location map, Figure 13-2 [MIZEX Group, 1986]. In the southernmost Greenland Sea in this image, newly formed ice is present at the northern edge of a large tongue of ice projecting eastward from the main ice edge approximately at the Greenland Fracture Zone.

The SAR image from the Barents Sea, Figure 13-1(c), acquired during the Seasonal Ice Zone Experiment, SIZEX'89 [SIZEX Group, 1989], shows characteristic ice features along the east coast of Svalbard, such as land-fast ice, shear zones, and polynyas. In the shear zone between the land-fast and drifting ice, the ice pack converges and forms large ridges in a belt along the coast. Adjacent to the shear zone, the transition from very large floes to small to medium floes is clearly seen.

SAR images can also be used to detect icebergs and evaluate their effects on the surrounding sea ice pack. For example, a SAR image, Figure 13-1(d), of the Barents Sea shows the interaction between grounded icebergs and the ice pack driven by the strong tidal current and mean ice advection [Johannessen et al., 1991b]. This interaction can be seen as tracks cut into the ice cover by icebergs. This is an important mechanism for fracturing large ice floes. Tracks are also generated by drifting icebergs due to the differential motion between the ice pack and the icebergs. The combined effects of this mechanism and the wave penetration causes the small size of ice floes in the western Barents Sea. The tracks left in the ice pack makes the detection of the icebergs easy.

On cloud-free days, infrared and visible-channel data from the Advanced Very High Resolution Radiometer (AVHRR) onboard the National Oceanic and Atmospheric Administration (NOAA) satellites provide images with 1-km resolution showing sea surface temperature and ice distribution. These images have revealed ice edge eddies, jets, and vortex-pairs along the ice edge of the Greenland Sea, Figure 13-1(e) [Johannessen et al., 1987]. The abundance of eddies (five overall) in this region show that eddies 1 through 4 strongly interact with the ice cover, while eddy 5 is seen to be an ocean eddy in the infrared image. However, the frequent occurrence of clouds in the SIZ makes it difficult to obtain a time series of images that can be used to study the dynamics of the ice edge region.

The images in Figure 13-1 are examples of an extensive data set collected in the Greenland and Barents Seas since 1978. In this chapter, we will review the main results accomplished during a decade of experiments that emphasized the use of microwave remote sensing techniques. In Section 13.2, the campaigns are summarized and the most important physical processes in the SIZ are presented. Recent modeling results of SIZ processes are summarized in Section 13.3. An example of regional ice forecasting using microwave observations is presented in Section 13.4, and in Section 13.5 the role of the SIZ in the climate system is discussed.

13.2 CAMPAIGNS

From 1979 to 1989, five major international field experiments were carried out in the Greenland Sea, Fram Strait,
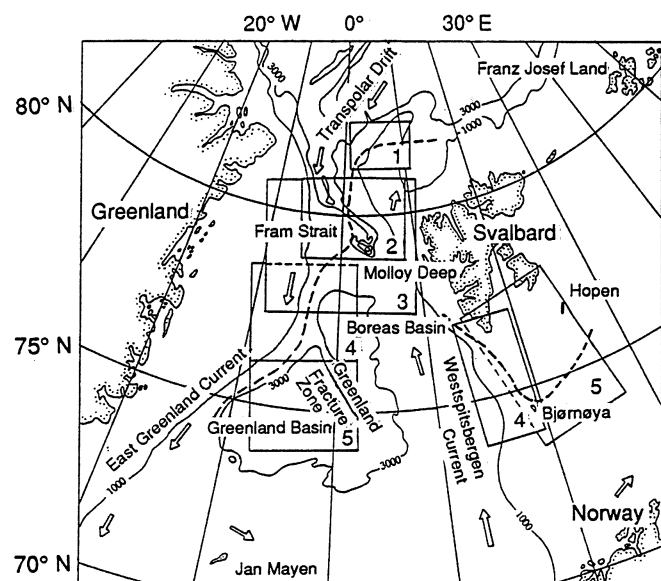

Fig. 13-2. Map showing the location of the major field experiments from 1979 to 1989: (1) NORSEX'79, (2) MIZEX'83, (3) MIZEX'84, (4) MIZEX'87, and (5) SIZEX'89. The arrows show the main currents and ice motion. The dashed lines indicate the mean ice edge location in the Greenland Sea during the summer experiments, and south of Svalbard during the winter experiments.

and Barents Sea: the Norwegian Remote Sensing Experiment, NORSEX'79 [Johannessen et al., 1983a]; the Marginal Ice Zone Experiments, MIZEX'83, MIZEX'84, and MIZEX'87 [Johannessen et al., 1983b; Johannessen, 1987]; and the Seasonal Ice Zone Experiment, SIZEX'89 [Johannessen et al., 1991a]. The locations of the experiments are shown in Figure 13-2, and a summary of the experiments' objectives and available sensors is presented in Table 13-1. A brief review of the oceanography of this region has been published by Johannessen [1986a].

The overall objectives of the experiments have been to improve our understanding of the air–ice–ocean processes

TABLE 13-1. Experiment objectives and available sensors.

Campaign	Objectives	Remote Sensing Observations
NORSEX'79 September–October 1979	1) The first study of mesoscale processes in the MIZ by combined remote sensing and in-situ observations. 2) Development of a passive microwave algorithm for ice concentration, ice types, and ice edge location.	Satellite: Nimbus-7 SMMR (every two days) Aircraft: CV-990: L-band SAR (two flights) C-130: passive radiometer and scatterometer Ship: Radiometer
MIZEX'83 June–August 1983	1) Pilot study of mesoscale physical and biological processes in the summer MIZ in the Fram Strait region. 2) Validation of active and passive microwave observation of ice and ocean processes in the summer MIZ.	Satellite: Nimbus-7 SMMR (every two days) Aircraft: CV-990: passive microwave imager and radiometer NRL-P3: passive microwave imager CCRS/ERIM CV-580: SAR Ship: Radiometer and scatterometer
MIZEX'84 June–August 1984	Extensive use of remote sensing techniques combined with in-situ measurements to study: 1) Ocean and ice circulation in the Greenland Sea during summer. 2) Mesoscale ice edge eddies. 3) Characteristics of summer ice. 4) Boundary layer meteorology. 5) Biological activity.	Satellite: Nimbus-7 SMMR (every two days) Aircraft: CV-990: passive microwave and imager radiometer NRL-P3: passive microwave imager and radiometers CCRS/ERIM CV-580: SAR CNES B-17: SLAR Ship: Radiometers and scatterometers
MIZEX'87 March–April 1987	1) Demonstrate the importance of daily SAR imagery in the study of ice–ocean eddies, ice motion, and other MIZ processes. 2) Study ice distribution, physical ice properties, water masses, deep water formation, boundary layer meteorology, biological activity, and ocean acoustics in the Greenland Sea in winter. 3) Carry out the first SAR study of the sea ice in the Barents Sea.	Satellite: Nimbus-7 SMMR (every two days) Aircraft: Intera X-band SAR (24 flights, three in the Barents Sea) NRL-P3: passive microwave imager Ship: Radiometers and scatterometers
SIZEX'89 Part 1 (The Barents Sea February 1989) SIZEX'89 Part 2 (The Greenland Sea March 1989)	1) Pre-ERS-1 validation of SAR ice parameters: ice concentration, ice kinematics, and ice types. 2) Demonstrate use of remote sensing data in ice forecasting. 3) Process studies: eddies, jets, vortex pairs, fronts, chimneys, deep water formation, and their influence on the ambient noise.	Satellite: DMSP SSM/I (daily) Aircraft: CCRS CV-580: SAR X- and C-bands ERIM/NADC P-3: SAR X-, C-, and L-bands Ship: Radiometers and scatterometers

in the SIZ and to develop and validate remote sensing techniques. During this decade, there has also been a development from basic research towards application and operational use of remote sensing techniques in sea ice monitoring and forecasting in the seasonal ice zone. One of the aims of this chapter is to present this development.

The concept and the strategy of all these experiments were to collect data from a three-level observational system—satellites, aircraft, and in-situ observations. During these experiments, data were collected from ice-strengthened vessels with helicopters, from operating inside the ice pack, from oceanographic research vessels operating in the open ocean adjacent to the ice edge, from drifting buoys tracked by the Argos system and bottom-moored buoys, and from aircraft and satellites. Instruments on these varied platforms acquired a diverse suite of ice, ocean, and atmospheric data.

13.2.1 NORSEX'79

The first remote sensing experiment in this series took place north and west of Svalbard in September and October 1979. Active and passive microwave instruments were used to study the location and structure of the ice edge, distribution of ice types, ice concentration, eddies, and ice edge upwelling in the seasonal ice zone region [NORSEX Group, 1983]. SAR imagery of the area was obtained for the first time using the NASA CV-990 L-band SAR with 25-m resolution. Two flights were performed: one on September 19 during easterly winds of 10 to 15 m/s parallel to the ice edge, and the next on October 1 when calm conditions had prevailed for the two preceding days (Figure 13-3).

On September 19, the SAR image showed a straight ice edge with several trailing ice plumes indicating the presence of a jet along the ice edge [Johannessen et al., 1983a]. Buoys drifting in the jet indicated a speed of up to 0.30 m/s along the ice edge. Sections of conductivity and temperature versus depth (CTD) obtained from the ship indicated upwelling outside the ice edge. During the calm wind situation of October 1, the SAR image showed the ice had a wavelike edge with approximate length scale of 20 to 40 km and several eddies with horizontal dimensions of 5 to 15 km. Johannessen et al. [1983a] showed that during these wind conditions the SAR image mirrored the ocean circulation.

Another aim of the experiment was to use the integrated data sets to develop and test an algorithm for estimating total and multiyear ice concentration from passive microwave measurements [NORSEX Group, 1983]. This set of emissivity observations from various ice types and water was used in the development of an algorithm [Svendsen et al., 1983] designed for use in the Greenland–Barents Seas SIZ. Comparison of simultaneous Nimbus 7 SMMR and aircraft data indicated that the total ice concentration in the experimental area could be estimated with an accuracy of ±3%, and multiyear ice concentration with ±10%. The geographical positioning of the ice concentration estimates, including the ice edge location, are accurate to ±10 km. The
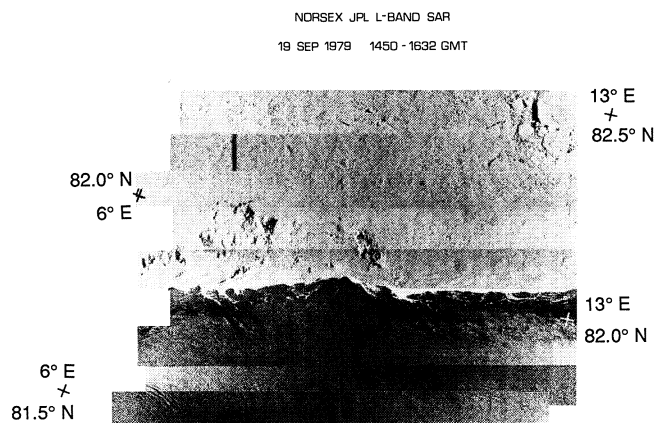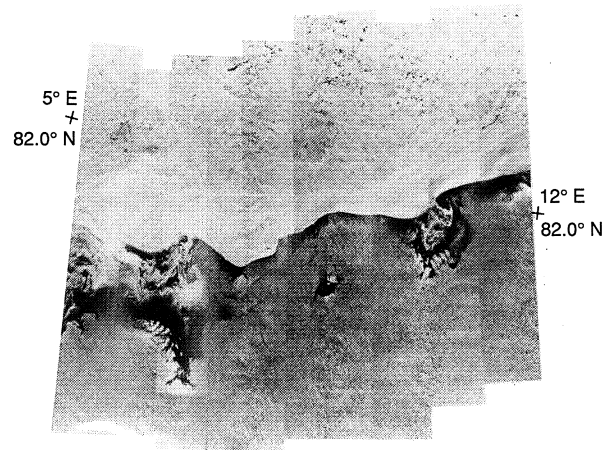

Fig. 13-3. Two airborne SAR mosaics obtained during NORSEX'79. The upper image is from October 1, 1979, when calm conditions had prevailed for the two preceding days. The lower image is from September 19, 1979, when easterly winds of 10 to 15 m/s blew parallel to the ice edge.

ice in this region varied from newly frozen, thin pancakes to snow-covered multiyear floes. During the experiment the snow cover remained dry, making the microwave signature of first- and multiyear ice clear [NORSEX Group, 1983].

13.2.2 MIZEX'83 and 84

NORSEX led to the creation of a more comprehensive and international program MIZEX, which consisted of a series of summer [MIZEX Group, 1989] and winter experiments [Johannessen, 1986b]. While NORSEX'79 focused on remote sensing and selected ice-ocean processes, the objective of MIZEX was a much broader attempt to improve our understanding of mesoscale air–ice–ocean interactive processes and the role they play in the climate system. In

addition to coordinated sea ice, oceanographic, meteorological, and remote sensing programs as carried out in NORSEX, MIZEX included acoustical and biological studies [MIZEX Group, 1986]. A comprehensive discussion of all aspects of these experiments is given in the thematic Marginal Ice Zone issues of the *Journal of Geophysical Research [92(C7)*, 1987, and *96(C3)*, 1991], and in *Polar Oceanography* by Muench [1990].

The remote sensing program obtained sequential synoptic images of the ice morphology and evolution of the ice edge region utilizing a variety of remote sensing aircraft and satellites. Of great importance in the execution of MIZEX was the ability to acquire real-time SMMR data from Nimbus 7, AVHRR data from the NOAA satellites, and airborne SAR data of the experiment areas. These observations were used to position the ships for mesoscale mapping. Remote sensing was also a key element in the oceanographic program that focused on obtaining a synoptic history of ocean currents and structure and to assess the role of fronts, eddies, and large-scale currents in the movement and decay of the marginal ice zone (MIZ). These field experiments were carried out in the Fram Strait–Greenland Sea region and the Bering Sea, however, emphasis was placed on the Fram Strait region because of its primary importance for the exchange of water, heat, and other quantities between the Arctic Ocean and the world's ocean.

The first MIZEX in the Fram Strait, which was a pilot for the main experiment in the summer of 1984, was carried out during a two-month period in the summer of 1983. This pilot experiment consisted of three major parts. The first was a study of the ice deformation of the interior of the MIZ [Leppäranta and Hibler, 1987] and internal waves [Sandven and Johannessen, 1987]. The second was a detailed study of the system of topographically controlled eddies in the Molloy Deep area [Johannessen et al., 1984b; MIZEX Group, 1986]. In the Fram Strait (Figure 13-4), warm water is carried northwards along the coast of Svalbard while sea ice and cold water are transported southwards in the western part of the Strait. In this dynamic region, eddies frequently occur and several were observed in the open ocean and along the ice edge (Figure 13-4). Over the Molloy Deep depression, a system of eddies were present. Deep CTD observations showed that these eddy signatures extended all the way to the bottom and thus were generated by the topography in the region. The third part of the experiment was an ice edge dynamics study south of the Molloy Deep based on transponder data transmitted from drifting ice buoys to the ship.

MIZEX'84 was the largest research program ever conducted in a marginal ice zone [Johannessen, 1987]. A multidisciplinary team of more than 200 scientists from 11 countries participated in the two-month experiment, which utilized seven ships, four helicopters, eight aircraft, and four satellite systems. A new experimental design, employed in MIZEX'84, utilized near-real-time remote sensing data acquired by aircraft and satellites to direct the ships to interesting ice-ocean features in which to deploy drifting Argos buoys, some with current meters below, and to obtain oceanographic and in-situ microwave observations. Figure 13-5(a) shows the aircraft SAR mosaic acquired on July 5, 1984. This image was used to direct ships to the eddy for in-situ observations and CTD profiles that were used to construct the three-dimensional eddy structure shown in Figure 13-5(c). An oblique aerial photograph, Figure 13-5(d), acquired at the same time as the SAR image, shows the surface manifestation of this eddy. Subsequent interpretation of the SAR image, Figure 13-5(b), shows the eddy along with other ice edge and ocean features.

The results from the MIZEX's [Campbell et al., 1987; Johannessen et al., 1987; Johannessen, J. A., et al., 1987] show that a number of eddies of 20 to 40 km dominate the mesoscale circulation in the Fram Strait. The rotational direction is mainly cyclonic and the maximum orbital speed is up to 0.40 m/s. Life times of these eddies have been observed to exceed 20 to 30 days. Some of the eddies remained stationary due to topographical trapping, while others propagated 10 to 15 km per day driven by the mean current. When these eddies propagate along the ice edge, ice is transported out into open water and warm water is advected into the ice pack, as accomplished by eddy 1 in Figure 13-1(e). Thus, the melting of the ice is enhanced and the ice edge can retreat 1 to 2 km per day due to the action of the eddies [Johannessen, J. A., et al., 1987].

While the aircraft SAR observations of the experimental area provided detailed information on the ice morphology at the mesoscale 30 to 100 km, the Nimbus 7 SMMR observations provided sequential information of the ice edge and ice concentration variations on a regional scale. A comparison of the aircraft active and passive microwave and visual observations with the SMMR ice concentration distributions indicates that for the summer MIZ the 30% isopleth correlates best with the actual ice edge position under diffuse conditions, while the 50% isopleth correlates best with a compact ice edge [Campbell et al., 1987]. Using these results, a composite of the derived SMMR ice edges for the experimental period (Figure 13-6) showed that the envelope of the edge variations is quite narrow, on the order of 50 km. This envelope correlates well with the shelf break south of 79° N, implying a strong regional topographical steering. Northeast of 79° N, the ice edge location is primarily determined by the inflow of warm Atlantic water [Johannessen et al., 1983a].

These results from the summer MIZEX'83 and '84 show the ability of active and passive microwave techniques to observe ice-ocean eddies and ice morphology during melting conditions. Physical processes are significantly different during the freezing season and one must understand both seasons to model the interannual variability of the MIZ. Complementary winter programs therefore took place in the Greenland and Barents Seas during March and April 1987 (MIZEX'87) and in February and March 1989 (SIZEX'89). SIZEX'89 was also an approved European Space Agency (ESA) prelaunch experiment for ERS-1 [Johannessen, 1986b].
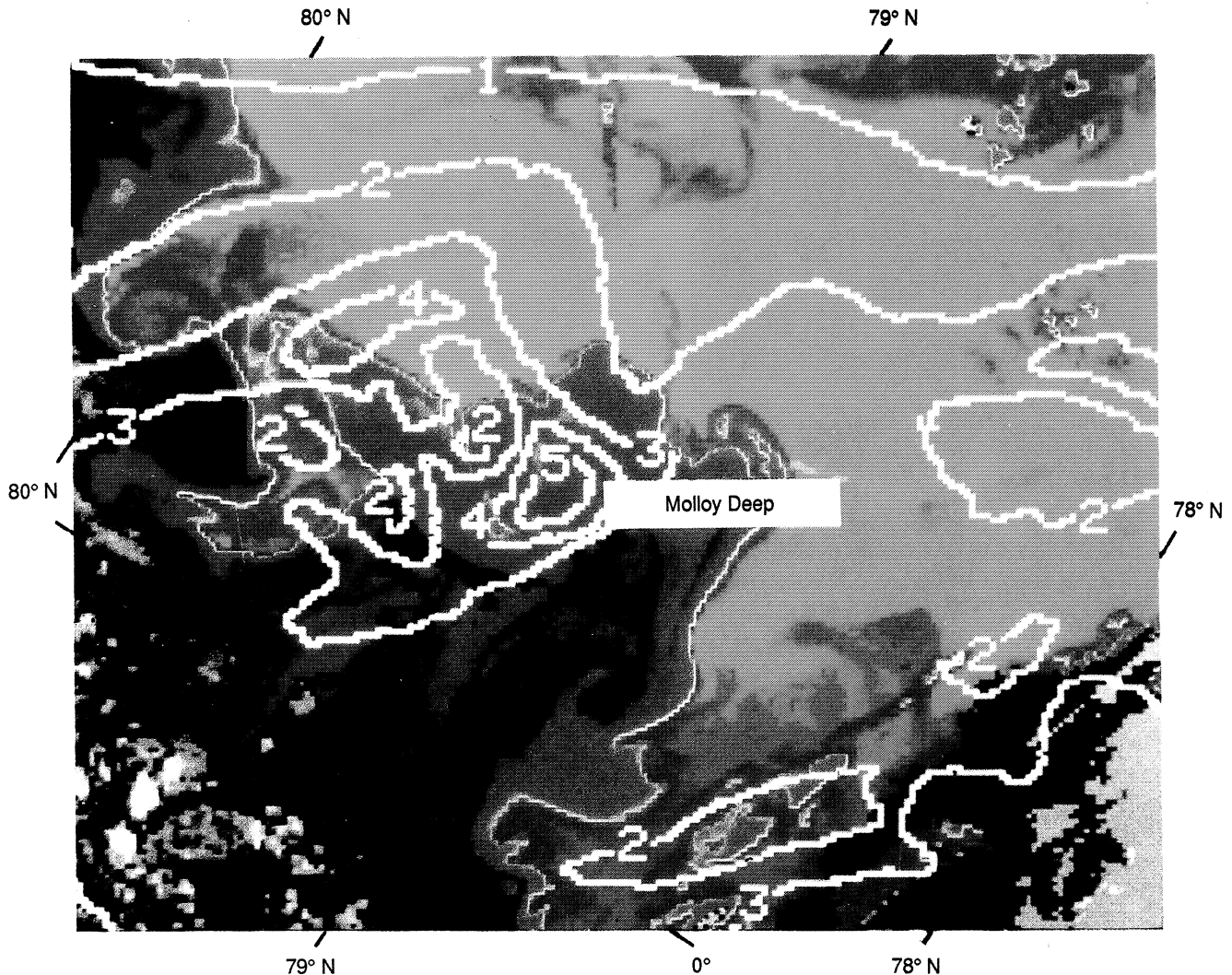
Fig. 13-4. NOAA AVHRR infrared image obtained in the Fram Strait during MIZEX'83. Yellow and red indicate warm water at 5° to 6°C, while blue represents a mixture of cold water and ice. The white lines show the bottom contours (for example, 1 indicates 1000 m).

13.2.3 MIZEX'87

The winter MIZEX'87 investigations were based on the need to understand the atmosphere–ice–ocean processes responsible for the advance of the winter ice edge and to validate the microwave remote sensing accuracies under conditions different from those in the summer.

MIZEX'87 was the first field experiment wherein daily regional SAR images were downlinked to the ship in real-time, which was essential to the execution of the experiment and efficient ship navigation in the ice. During the experiment, a total of 24 SAR flights were completed, 13 of which were on consecutive days in the Greenland Sea and three in the Barents Sea [MIZEX Group, 1989]. The previous experiments had shown the importance of having SAR coverage of the same area every day in order to map the

rapid changes of the ice edge characteristics [Campbell et al., 1987].

In Figure 13-7, a unique sequence of 12 images from March 28 to April 8 is shown for the first time. The salient feature of this sequence is the extreme structural variability of the ice edge at the daily time scale. The cause for this is the evolution of eddies, jets, and vortex-pairs that are modified by wind and surface wave variations.

What follows is a description of each mosaic of the location and evolution of key ocean and ice events. On March 28, slightly north of the center of the mosaic, an ice tongue extended eastwards from the ice edge opposing a northeasterly wind of 6 m/s. South of this tongue, an anticyclonic eddy was indicated. Twelve hours later, when the wind had decreased to 3 m/s from the north, this anticyclonic eddy was clearly shown with a diameter of
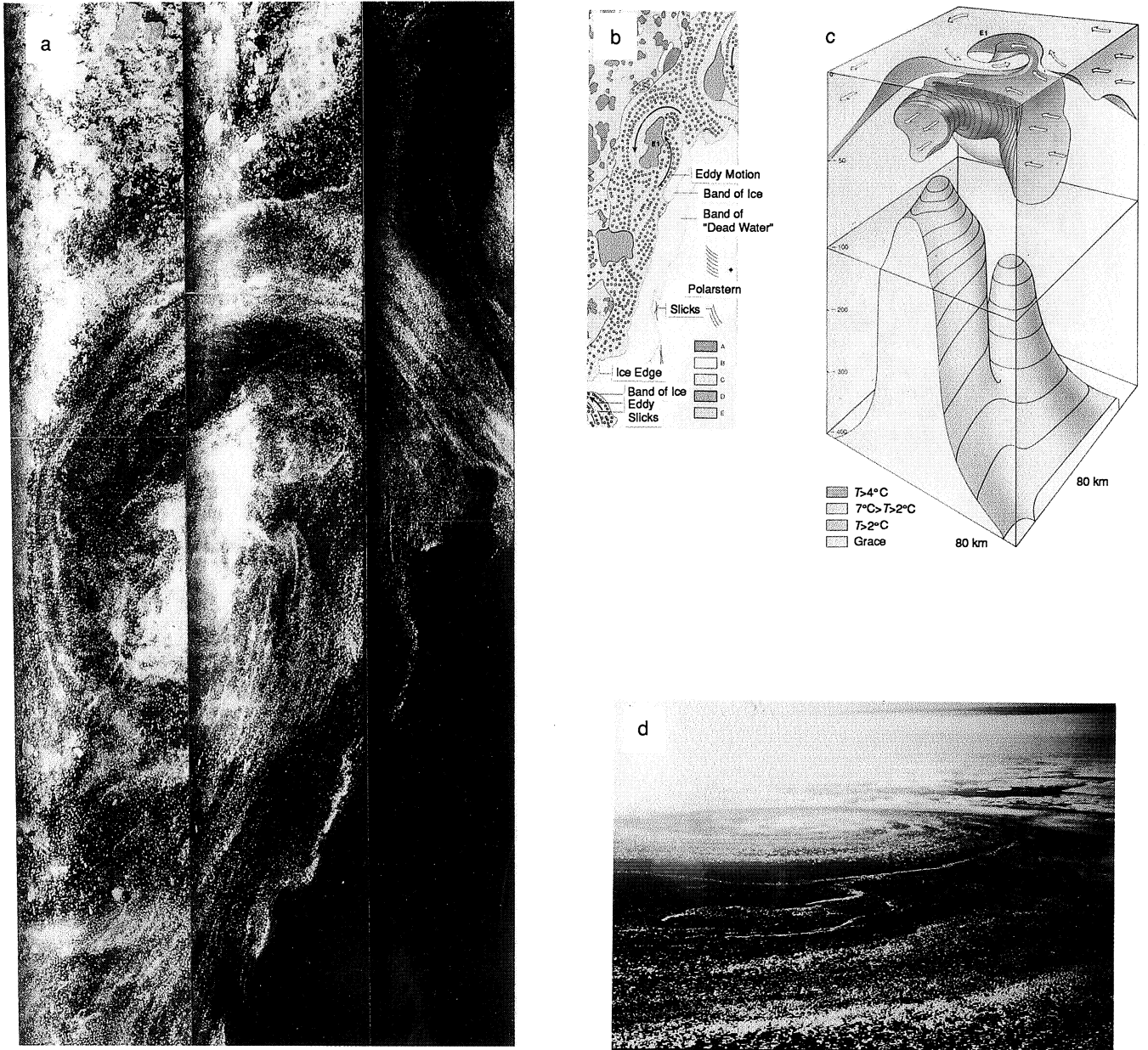
Fig. 13-5. (a) Aircraft SAR image acquired on July 5, 1984, of a cyclonic ice edge eddy in the Greenland Sea. (b) Interpretation of the whole SAR mosaic. (c) Three-dimensional structure of the eddy obtained from CTD sections. (d) Oblique aerial photograph of the eddy.
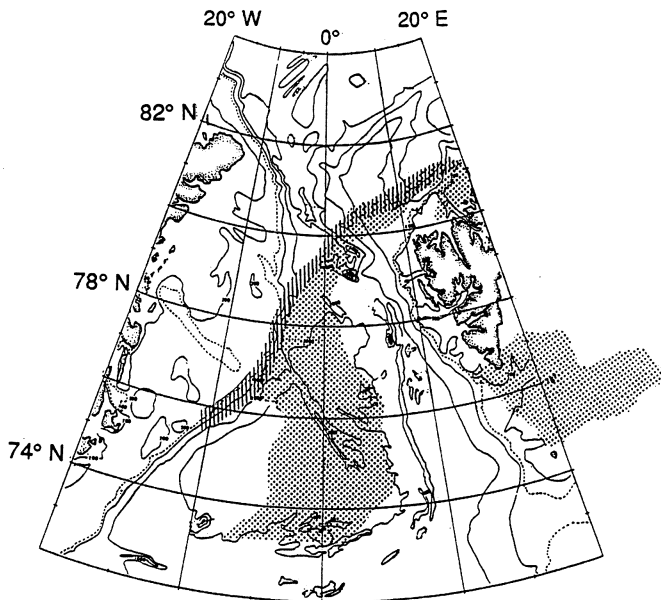
Fig. 13-6. Envelope of ice edge positions observed by SMMR during the summer experiment MIZEZ'84, ice edge variations are typically within a 60-km range (hatched area) and during the winter experiment MIZEX'87 (dotted area).

approximately 40 km. At this time the tongue to the north of the anticyclonic eddy had evolved into a jet with a vortex-pair less than 20 km. In the northern part of this image, the system of eddies over the Molloy Deep is clearly seen, as well as new ice freezing in the southern part of the image. This image serves as an excellent example of how the ice floes mirror the complex mesoscale ocean circulation under moderate to light wind conditions. Such phenomena can only be observed by sequential SAR images.

During the next several days from March 30 to April 2, the wind varied from 6 to 8 m/s between the north and the northeast. In these images, the ice edge was meandering and was compact due to the on-ice wind forcing and surface wave radiation pressure. In spite of the on-ice wind forcing on March 31, a new tongue evolved below the center of the image and projected eastwards. During the next two days, this tongue evolved and was advected to the south. Note that at the extreme end of this tongue a small vortex-pair was observed on March 31 and April 1. On April 2, in the center of the mosaic, a cyclonic eddy was present, extending into the ice pack. In the southern part, a new jet with the indication of a vortex-pair was present. During the next four days the wind decreased to 4 m/s, and this caused the ice pack to relax and once again mirror the mesoscale ocean circulation. The vortex-pair that was present in the southern part on April 2 evolved into a large anticyclonic eddy with a diameter of approximately 60 km, which persisted until April 6.

During this experiment, the smaller eddies and vortex-pairs clearly seen in the SAR mosaics were also documented

by CTD observations, which were composed of polar surface water plumes extending from the ice edge. On April 5, a smaller tongue of ice projected southwestwards from the center of the 60-km anticyclonic eddy to form a new vortex-pair, which was clearly seen on April 6. North of this eddy several jets and vortex-pairs projected eastwards from the ice edge on April 6, revealing exceptionally energetic mesoscale ocean circulation. This condition persisted throughout the following three days.

Downlinking SAR information enabled us to acquire a CTD section of this anticyclonic eddy, Figure 13-8. The fields of salinity and density show this eddy extended to the bottom. The geostrophic velocity field computed from these data, Figure 13-8(d), and velocities obtained by drifting buoys verified the anticyclonic nature of this eddy. This section across the eddy center indicated a core of warm Atlantic intermediate water that circulated in the eddy between 100 and 200 m depth. The generation of this anticyclonic eddy can be explained by conservation of potential vorticity as the East Greenland current passed over a major ridge, the Greenland fracture zone.

The April 6 image shows the greatest number of eddies, jets, and vortex-pairs. The entire ice edge, approximately 300-km long, is composed of these energetic mesoscale phenomena. On April 7 and 8, the ice morphology is similarly complex but less structured than on April 6. On April 7 and 8, in the southwest of each image large fields of ice plumes composed of grease ice and small pancakes appeared, indicating active freezing. These are potential areas of convection driven by brine exclusion. In our long experience of acquiring SAR images during NORSEX, MIZEX, and SIZEX, the April 6 image is the most complex we have ever obtained and presents a major challenge to the modeling community.

In general, the ice edge region is characterized by a 20- to 30-km wide zone of a bright SAR signature. In-situ observations established that this zone consists of broken-up floes of mainly multiyear ice with rough surfaces and edges that cause high backscatter from the SAR. In this zone, individual floes cannot be identified. The band pattern is indicative of strong horizontal velocity shear. Inside the ice edge zone, the most predominant feature is the occurrence of large multiyear floes of high backscatter that are broken into pieces. Between the multiyear floes, thin new-frozen ice with low backscatter is found. By comparing consecutive mosaics, the interior of the pack ice is observed to drift southwards at a speed of about 20 km per day, while the velocity of the ice edge is 30 to 40 km per day. This ice edge jet is caused by the baroclinicity associated with the East Greenland polar front, the frontal boundary between the cold, fresh waters of the East Greenland current and the warmer, more saline Atlantic intermediate water seaward of the ice edge. This ice edge jet is enhanced during northerly winds because of the higher atmospheric drag coefficient over the rough ice edge zone [Guest and Davidson, 1987]. Similar jets were observed during NORSEX'79 [Johannessen et al., 1983a].
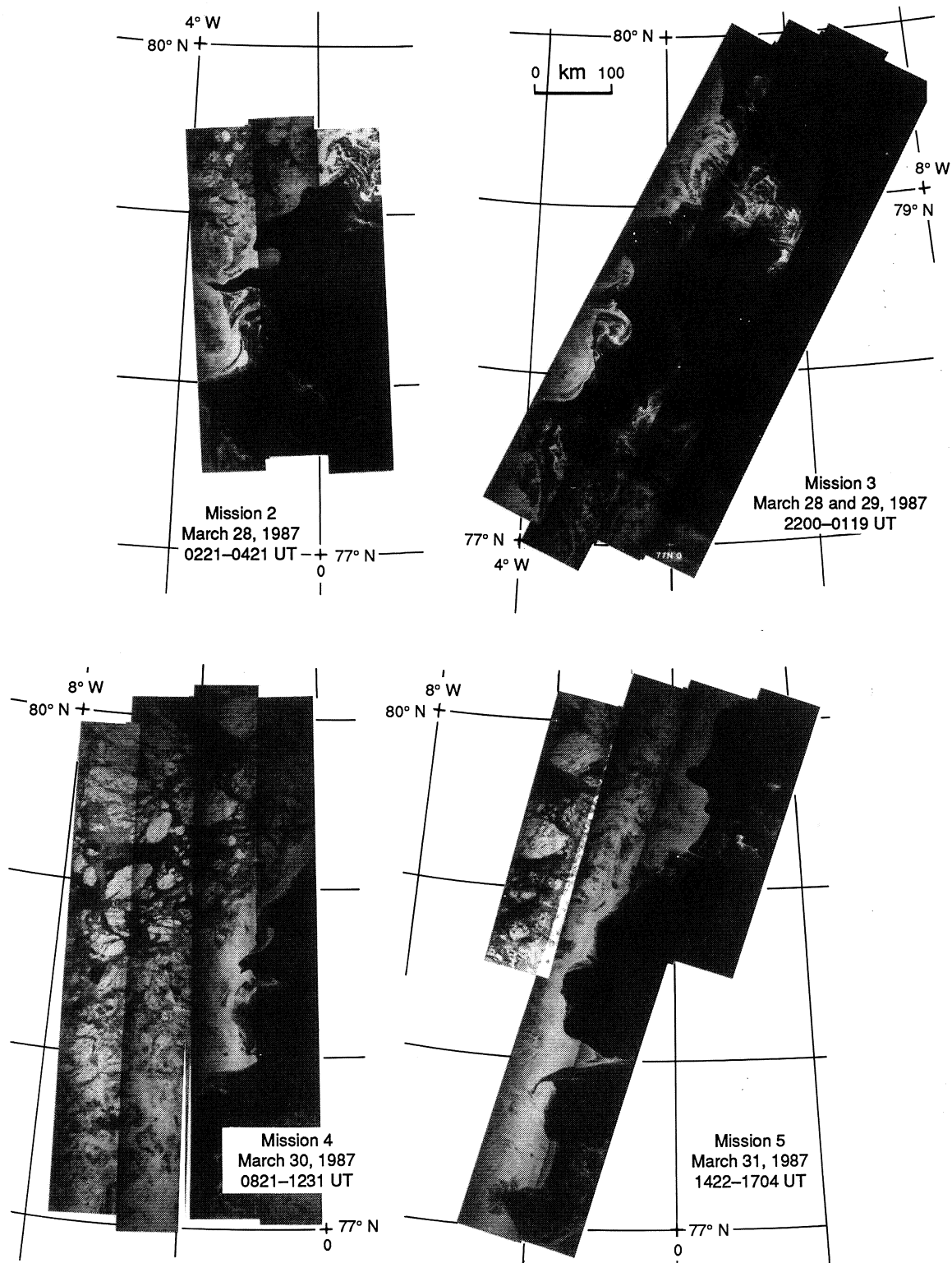
4° W
80° N

Mission 2
March 28, 1987
0221–0421 UT + 77° N
0

0 km 100

80° N

8° W
79° N

77° N
4° W

Mission 3
March 28 and 29, 1987
2200–0119 UT

8° W
80° N

Mission 4
March 30, 1987
0821–1231 UT

77° N
0

8° W
80° N

Mission 5
March 31, 1987
1422–1704 UT

77° N
0

Fig. 13-7. Sequence of 12 SAR images in the Greenland Sea obtained from March 28 to April 8, 1987.

4° W
80° N +

Mission 7
April 1, 1987
1619–1846 UT

0 km 100

Mission 8
April 2, 1987
1044–1350 UT

+ 77° N
0

8° W
80° N +

Mission 11
April 3, 1987
1714–2000 UT

76° N
+
0

8° W
78° N +

Mission 12
April 4, 1987
1800–2145 UT

76° N
0

Fig. 13-7. Sequence of 12 SAR images in the Greenland Sea obtained from March 28 to April 8, 1987. (Continued)
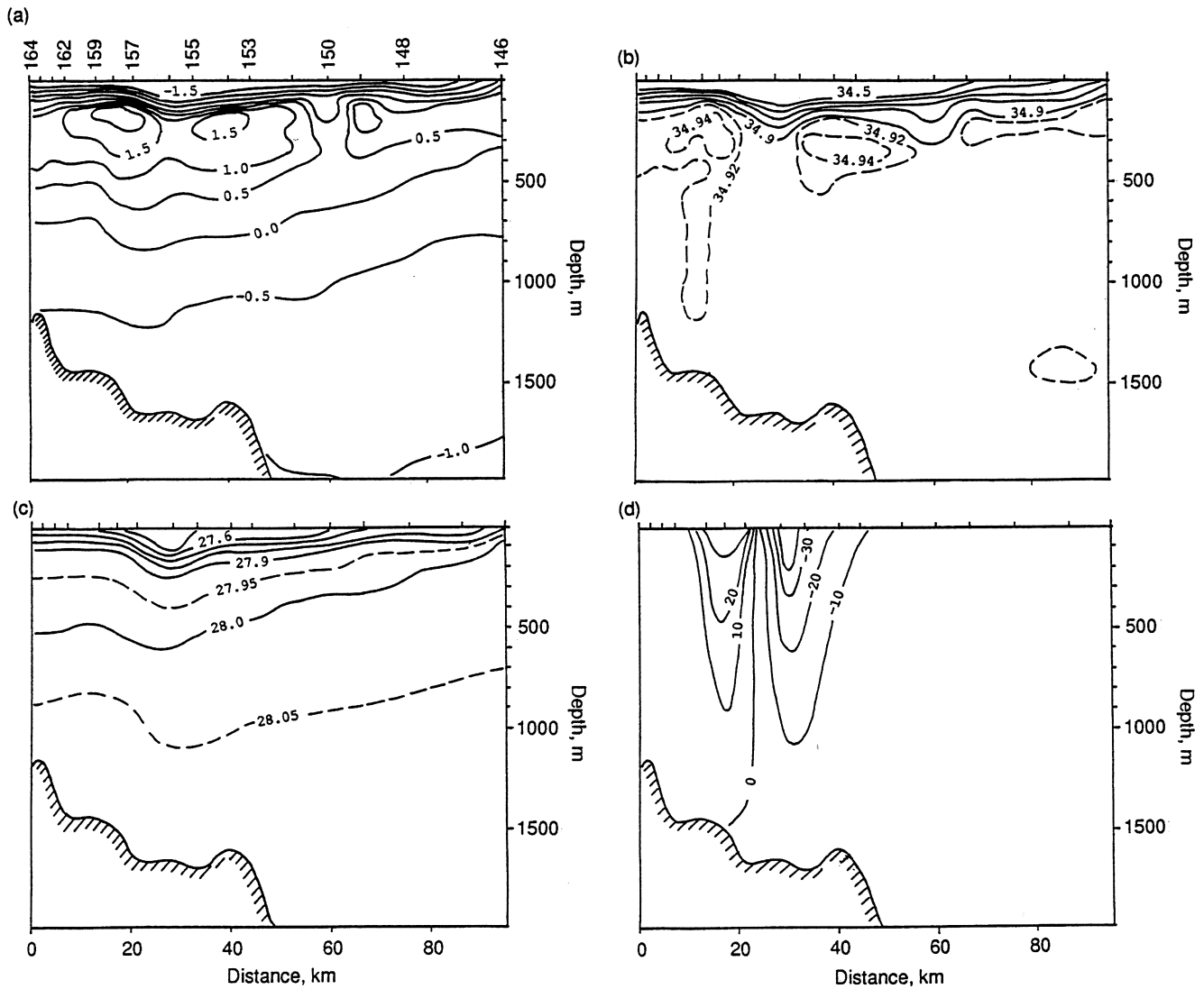
Mission 14
April 5, 1987
1740–2100 UT

Mission 15
April 6, 1987
1230–1426 UT

Mission 16
April 7, 1987
1200–1420 UT

Mission 18
April 8, 1987
1328–1700 UT

8° W
79° N

0   km   100

79° N

77° N
0

12° W
79° N

77° N
0

77° N

Fig. 13-7. Sequence of 12 SAR images in the Greenland Sea obtained from March 28 to April 8, 1987. (Continued)

(a)

(b)

(c)
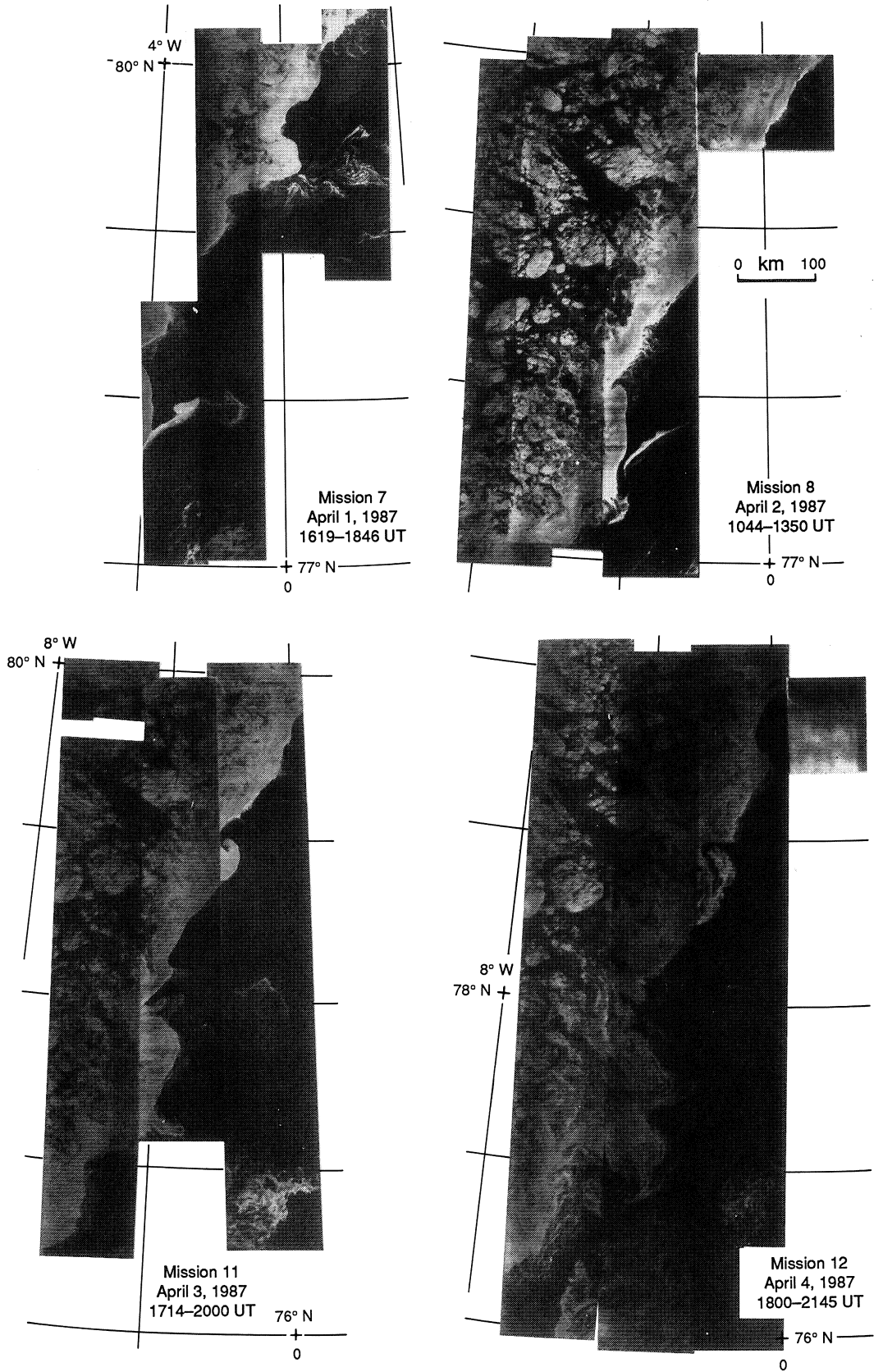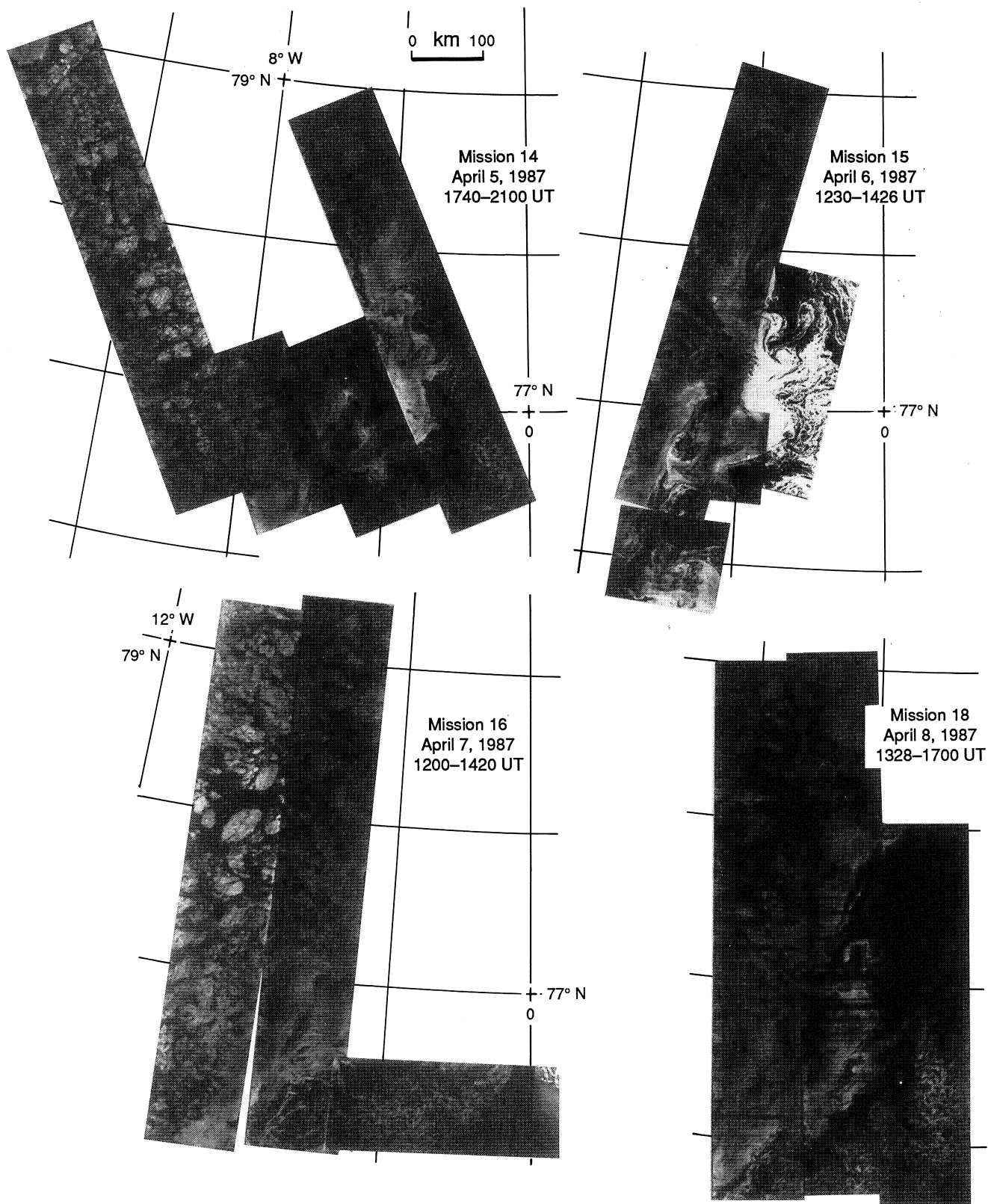
(d)

Fig. 13-8. (a) The vertical section of temperature in degrees Celsius, (b) salinity in parts per thousand, (c) potential density in sigma-theta, and (d) geostrophic velocity in cm/s across the anticyclonic eddy shown in the SAR images of April 4 and 5. Positive values of the geostrophic velocity indicate flow into the page, negative values out of the page.

Regional observations of the SIZ were accomplished with SMMR data. A sequence of nine SMMR images from the Greenland and Barents Seas from March 1 to April 10 is shown in Figure 13-9. Even at this coarse resolution (25 km), the extremely dynamic nature of the SIZ can be observed on a regional scale much larger than the mesoscale of the SAR images. It is interesting to compare these images with the SAR images presented above in Figure 13-7. For example, on March 29 the large area of ice plumes in the southern part of the SAR image (Figure 13-7) appears in the SMMR image as a tongue of low-concentration ice projecting from the ice pack eastwards at 77° N. This ice tongue is most clearly seen in the SMMR data on March 31.

This sequence of SMMR images also serves to illustrate how different the ice edge morphologies in winter are from those in summer. For example, from March 1 through 31 a large area of ice projected eastward towards Svalbard with the ice edges far east of those found during the summer, as can be seen in the comparison of the winter and summer envelopes of ice edge positions shown in Figure 13-6. By comparing these envelopes with the bathymetry, it can be seen that the winter ice-edge positions are not forced by the bottom topography as are the summer positions. Rather, the eastern extent of the ice edge during winter is determined by the location of the polar ocean front in the Greenland Sea [Johannessen, 1986a].
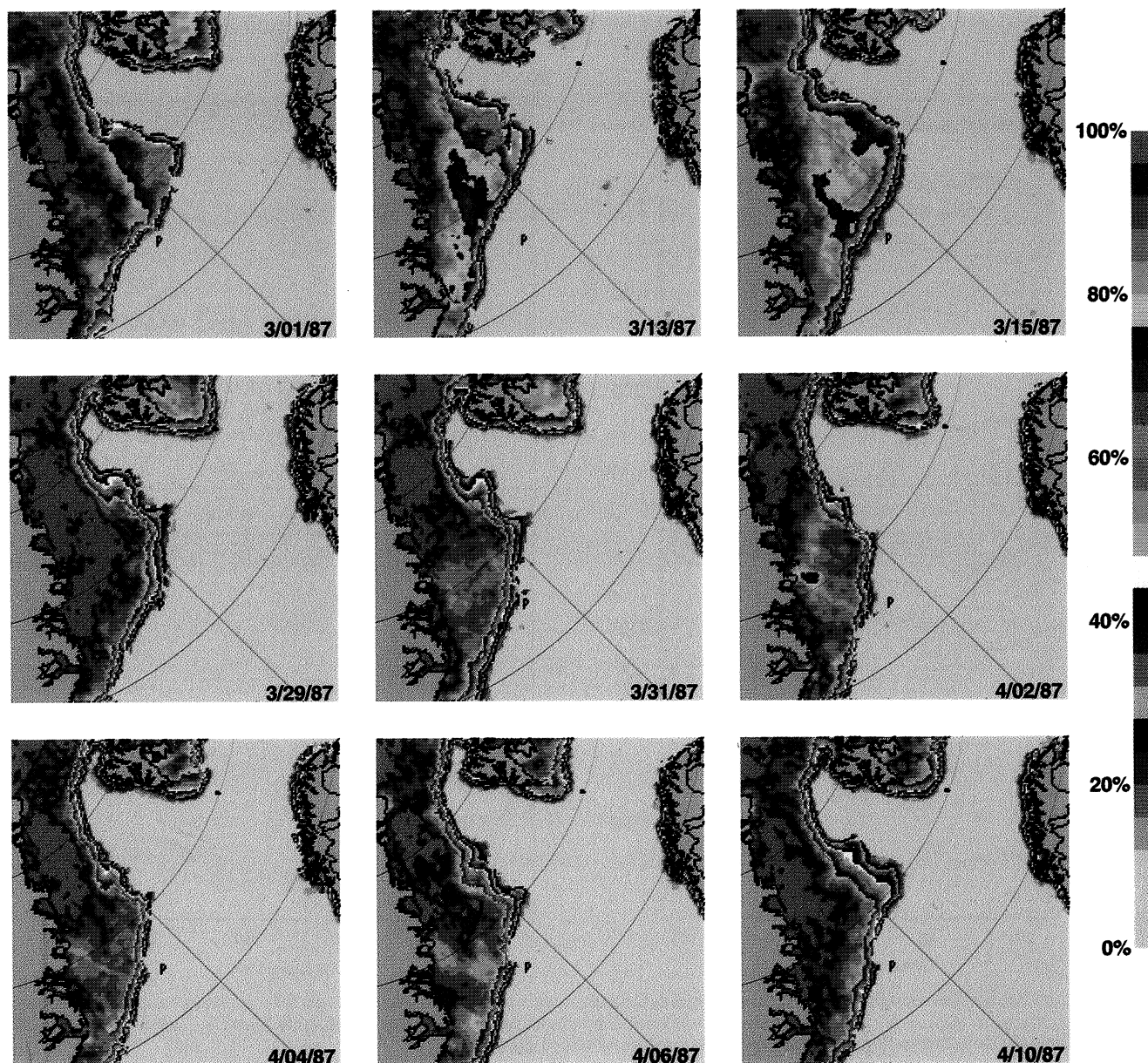
Fig. 13-9. A sequence of SMMR images of the Greenland and Barents Sea obtained during MIZEX'87 from March 1 to April 10. The vertical bar gives the color code for the derived ice concentrations.

During the winter, the western Barents Sea is primarily divided into a warm and cold part, separated by the Bear Island polar front located at the shelf break near Bjørnøya (Figure 13-2). This division is caused by the inflow of warm Atlantic water and the outflow of cold polar water along the shelf between Hopen and Bjørnøya [Johannessen and Foster, 1978]. When cold polar air flows southward, rapid freezing of new ice occurs over large areas. When warm air is advected in from the south by rapidly moving low pressure systems, this new ice is destroyed by melting and wave action. Some of these rapid advances in ice growth can be seen in the sequence of SMMR images shown in Figure 13-9,

especially during March. The southern limit of the ice edge in the Bjørnøya region coincides with the warm boundary of the Bear Island polar front. When the ice is forced across this front, it will quickly melt in the warm Atlantic water.

The first SAR mosaics of the Barents Sea were obtained during MIZEX'87 (Figure 13-10) starting on April 9, 1987 [Sandven and Johannessen, 1992]. They provided detailed information on the ice edge morphology and processes, as well as ice floe distribution, ice concentration, and ice motion. A pronounced feature in the mosaics is the rapid growth of an ice jet that developed into a vortex-pair near the southern tip of Svalbard. This information, coupled
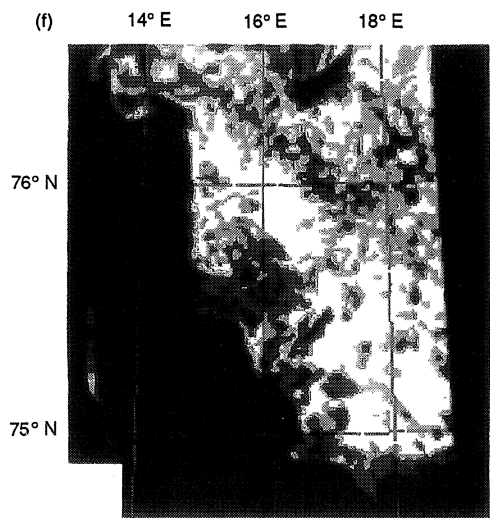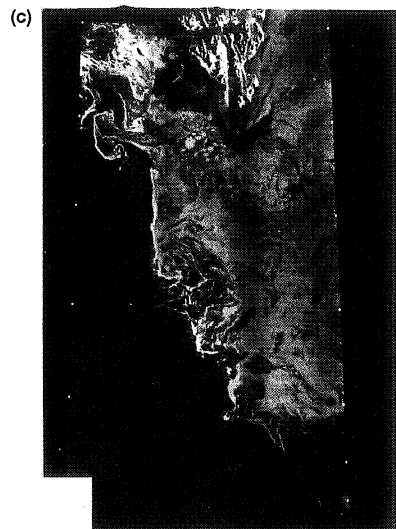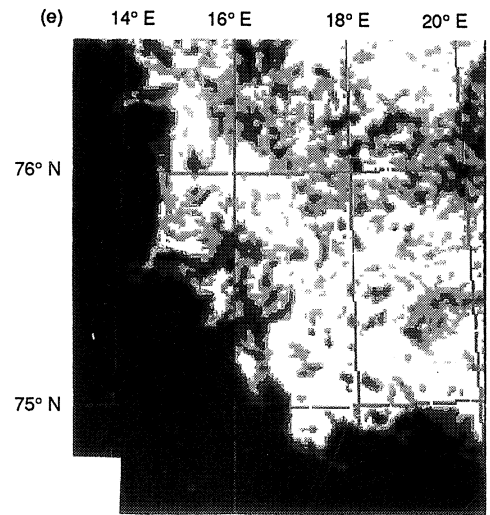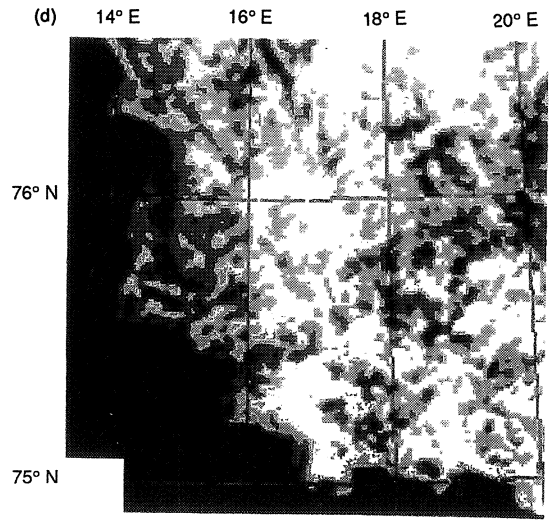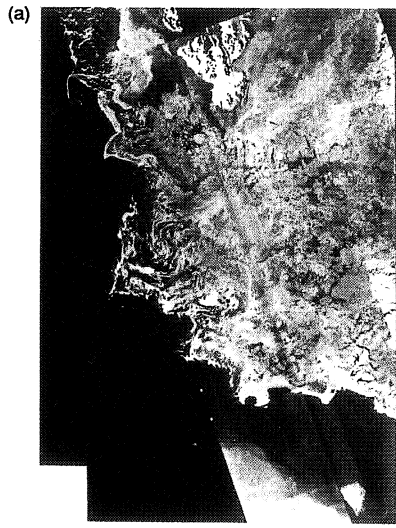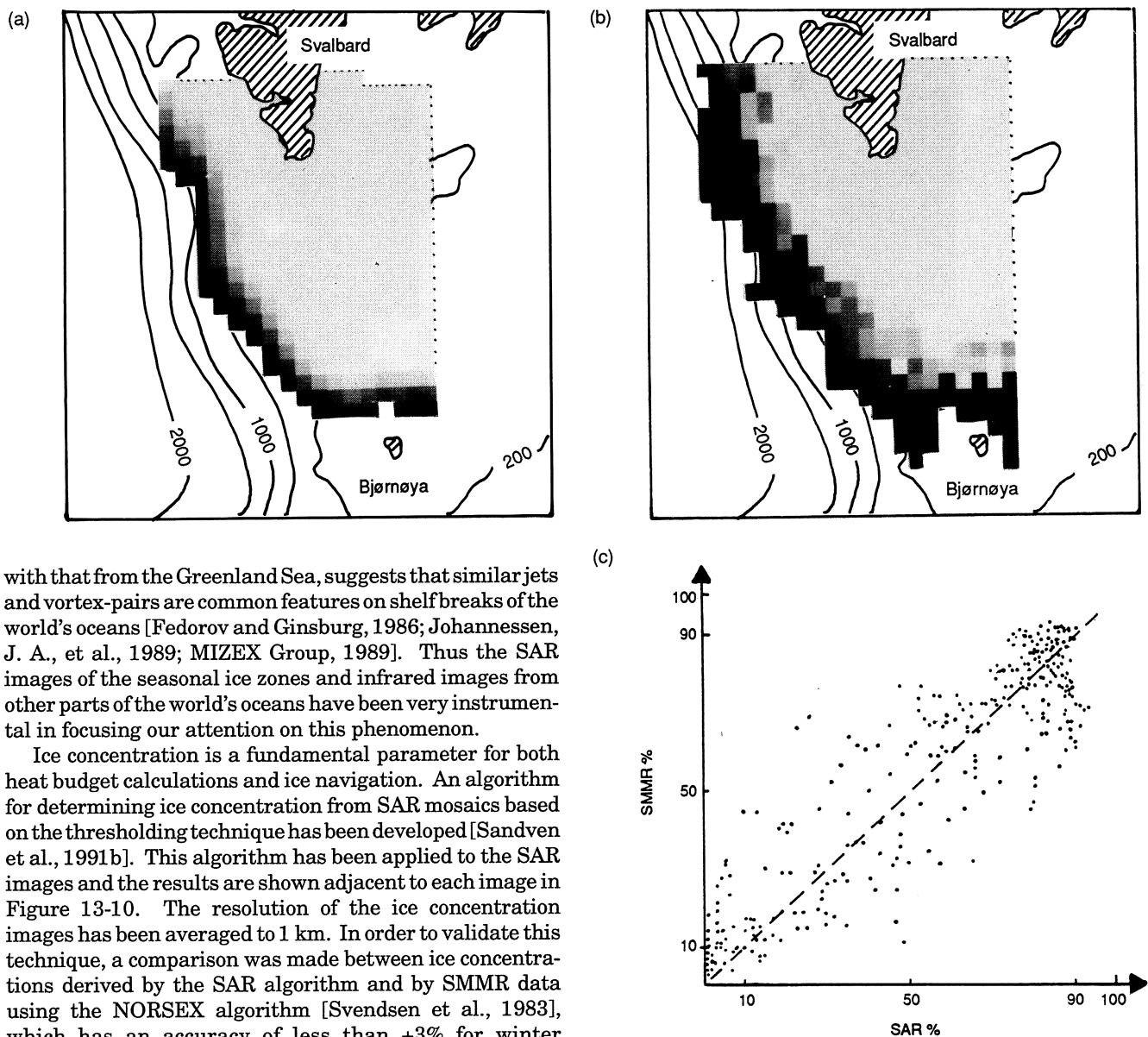
Fig. 13-10. Three SAR images obtained in the Barents Sea during MIZEX'87 on (a) April 9, (b) April 10, and (c) April 11. For each SAR image, the ice concentration is estimated using the algorithm proposed by Sandven et al. [1991b] is shown to the right of the image. White indicates ice concentration above 90%, orange from 70% to 90%, and light blue from 50% to 70%.

(a)

(b)

with that from the Greenland Sea, suggests that similar jets and vortex-pairs are common features on shelf breaks of the world's oceans [Fedorov and Ginsburg, 1986; Johannessen, J. A., et al., 1989; MIZEX Group, 1989]. Thus the SAR images of the seasonal ice zones and infrared images from other parts of the world's oceans have been very instrumental in focusing our attention on this phenomenon.

Ice concentration is a fundamental parameter for both heat budget calculations and ice navigation. An algorithm for determining ice concentration from SAR mosaics based on the thresholding technique has been developed [Sandven et al., 1991b]. This algorithm has been applied to the SAR images and the results are shown adjacent to each image in Figure 13-10. The resolution of the ice concentration images has been averaged to 1 km. In order to validate this technique, a comparison was made between ice concentrations derived by the SAR algorithm and by SMMR data using the NORSEX algorithm [Svendsen et al., 1983], which has an accuracy of less than +3% for winter conditions in the MIZ. Since the resolutions of SAR and SMMR are very different, a common pixel size of 12 km was used. A comparison between the two algorithms, shown in Figure 13-11, indicates that the SAR ice concentration estimates have an accuracy on the order of 20%. These results are promising for the application of SAR ice concentrations in operational ice monitoring and forecasting, but need to be improved for heat flux estimates in climate studies.

13.2.4 SIZEX'89

The SIZEX program was accepted by ESA as a key ice validation program for the first European Remote Sensing Satellite (ERS-1). A prelaunch experiment, SIZEX'89, was carried out in the Barents and Greenland Seas during

(c)

Fig. 13-11. Two images of ice concentration from April 10, 1987, in the Barents Sea, are superimposed on a bathymetric map, and displayed by a gray-scale ranging from black (10% to 20% concentration) to white (>90% concentration). (a) Ice concentration derived from the SAR image, averaged to a resolution of 12 km; (b) ice concentration derived from SMMR data using the same resolution as above; and (c) a scatter diagram of the two estimates.

February and March 1989. It was the first major seasonal ice zone experiment in a shallow water region with strong tidal currents.

The ERS-1 SAR C-band was simulated by flying the Canadian Centre for Remote Sensing X- and C-band SAR onboard the CV-580 every third day, which was the ERS-1 repetition cycle for the ice phase from January 1 to March

31, 1992 [SIZEX Group, 1989]. Figure 13-12 shows the experiment area, the ice edge positions derived from SSM/I and AVHRR, selected buoy tracks, current vectors near the ice edge, and ship tracks where oceanographic data were obtained.

The four mosaics from February 17, 20, 23, and 26, which covered the ice edge region from about 18° E to 23° E, provide detailed information about ice features, bands, tongues, and eddies (Figure 13-13). In general, there are characteristic differences in ice edge conditions between the western Barents Sea, from Bjørnøya to Spitzbergen, and the area east of Bjørnøya. East of Bjørnøya the ice edge region usually consists of fairly compact ice, except for a few nautical miles near open ocean. Outside the main ice edge, relatively cold water, which is favorable for freezing in winter, is present. This cold water is, however, usually confined to the shelf region shallower than 100 to 200 m and limited by the Bear Island polar front, which inhibits freezing south of the slope of the Bjørnøya Channel and the shelf break between Bjørnøya and Spitzbergen, as discussed in Section 13.2.3. Between Bjørnøya and Spitzbergen, the ice that drifts towards the open ocean, as shown by the Argos buoys drift (Figure 13-12) and SAR-derived ice kinematics, rapidly melts when it comes in contact with the warmer Westspitzbergen current. Some of the ice is transported northwards along the west coast of Spitzbergen where it eventually melts.

In this section we describe and quantify some of the characteristic ice features observed in these SAR images. The results have been presented by Sandven et al. [1991a] and are summarized in Table 13-2. The most pronounced
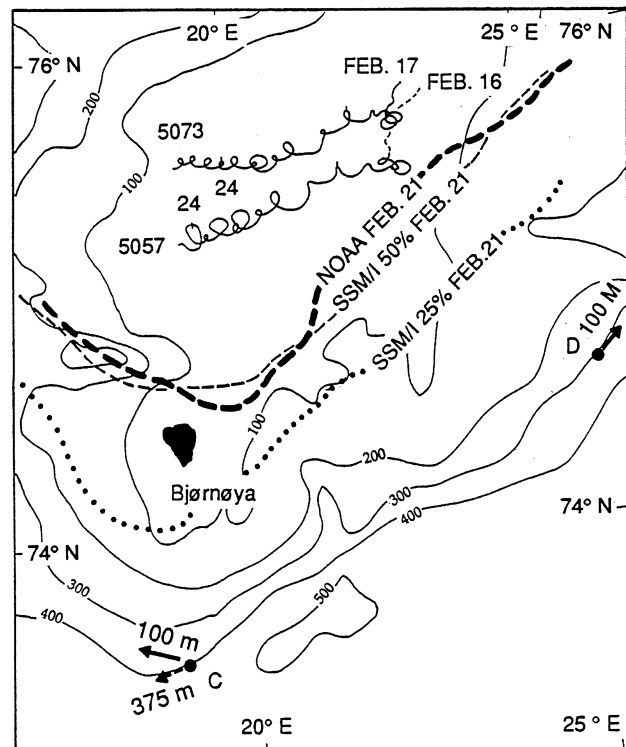

Fig. 13-12. Map of the SIZEX'89 experiment area in the Barents Sea during February. The ice edge positions from NOAA AVHRR and SSM/I are shown in bold dashed and dotted lines, respectively, the trajectories of two drifting ice buoys (5057 and 5073) are shown for the period from February 16 to 25. Two bottom-moored current meters are indicated with vectors illustrating the mean current at 100 m (mooring D) and 100 and 375 m (mooring C).

TABLE 13-2. Quantification of ice features.

Feature	Reference in Figure 13-13	Length, km	Width, km	Orientation/ Location	Time scale, days	Motion
Bands outside the ice edge	1	5–30	0.2–5	Mostly N–S meanders	<3	Propagating
Zones of reduced ice concentration inside the ice edge (leads)	2	5–30	0.5–5	Mostly N–S meanders	1–5?	Westward 10 km/day
Bights	3	20–50	20–50	E of Bjørnøya NW of Bjørnøya	Permanent? Permanent?	Stationary stationary
Tongues	4	20–50	10–20	NS at 23° E NS at 19° E	? 2–5?	Stationary propagating
Eddies	5	5–15	5–15	Around Bjørnøya 23° E	1–2? ?	Propagating ?
Polynyas	6	20–30	20–30	Hopen area	10	Westward propagation
Tracks produced by grounded icebergs	7	10–50	0.100–0.200	Ellipses from Bjørnøya to Hopen	1–3	Propagating
Fronts	8	>20	≈0.100	NE along the Bjørnøya Channel, S and W of Bjørnøya	Permanent	Stationary
Internal waves	9	Wavelength 1–3		E of Bjørnøya	<3	Propagating

(a)   (b)

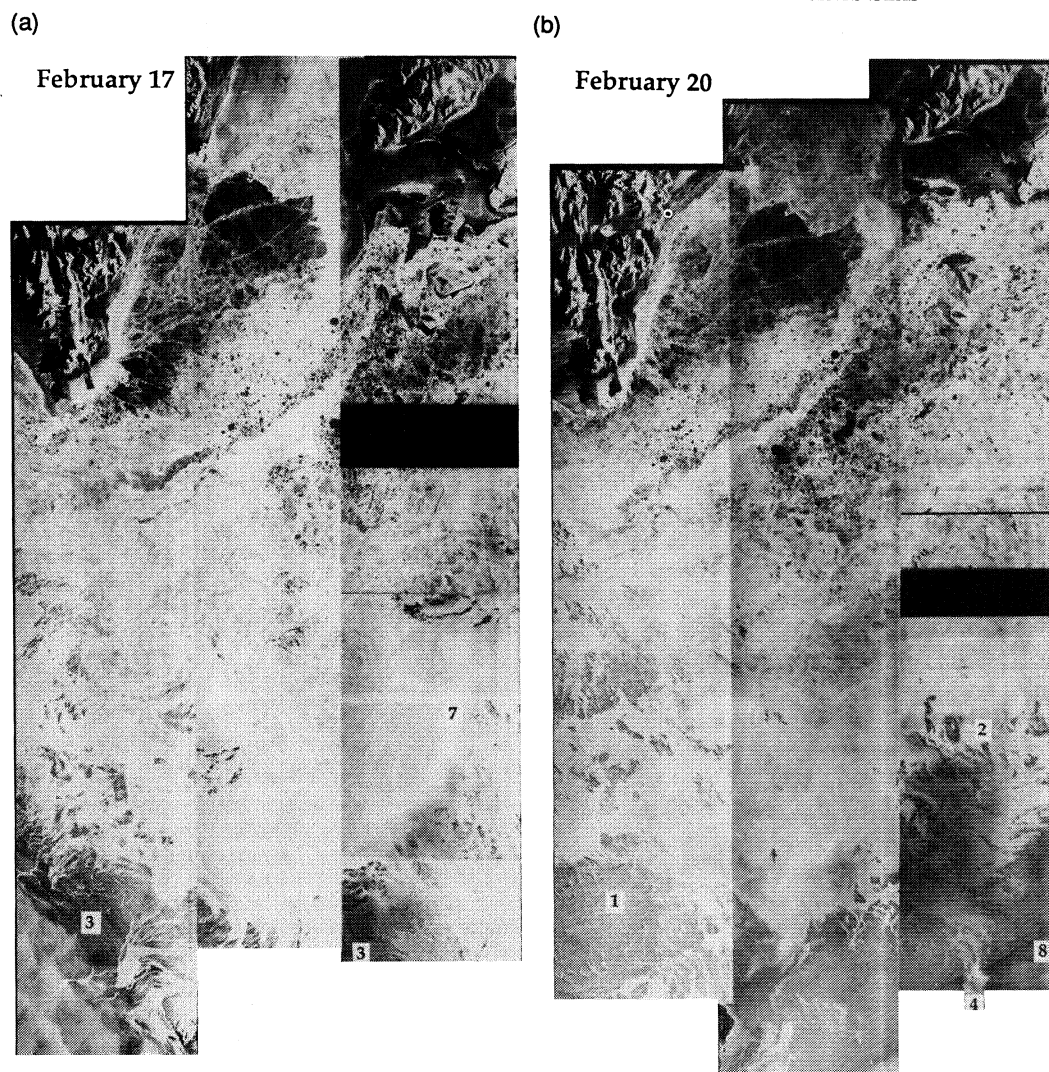February 17   February 20

Fig. 13-13. SAR mosaics obtained during SIZEX'89 on (a) February 17, (b) February 20, (c) February 23, and (d) February 26.

features are bands of ice outside the main edge, indicated by the number 1 in the mosaics of Figure 13-13. East of Bjørnøya these bands extended out from the ice edge and were oriented normal to the wind direction. West of Bjørnøya the bands were also normal to the wind direction, but along the ice edge. None of the ice bands observed on February 23 could be recognized three days later. In spite of moderate winds during this period, the ice bands changed rapidly, implying that their life times were less than three days. The typical length of the bands was from 5 to 30 km and the width varied from 100 m to 2 km.

While ice bands outside of the edge of the pack are a prominent feature in these mosaics, elongated zones of reduced ice concentration were observed inside the main ice edge, denoted by the number 2 in the mosaics of Figure 13-13. These zones are identified by darker signatures, indicative of areas with lower ice concentration or thin ice, and had a prevailing north–south orientation with consid-

erable meanders. Their length scale was similar when compared to the bands outside the ice edge, while their widths were larger. Two of the larger zones observed on February 23 can be recognized three days later. They had moved about 30 km westwards in three days. Such ice zones can also reflect some of the ocean circulation in the area, such as tidal currents and eddies.

A characteristic feature in all the mosaics is a bight of open water with scattered ice bands to the north of Bjørnøya, located by the number 3 in the mosaics of Figure 13-13. This bight has a horizontal scale varying from 20 to 50 km. A second bight is found east of Bjørnøya on February 17 and 20, with a diameter of 50 to 60 km. In the two last mosaics, this bight becomes less pronounced. The bights are associated with submarine troughs, which are filled with warmer water. The bights are therefore stationary and probably a permanent feature when the mean ice edge is located in the same position as in February 1989. These bights, which are
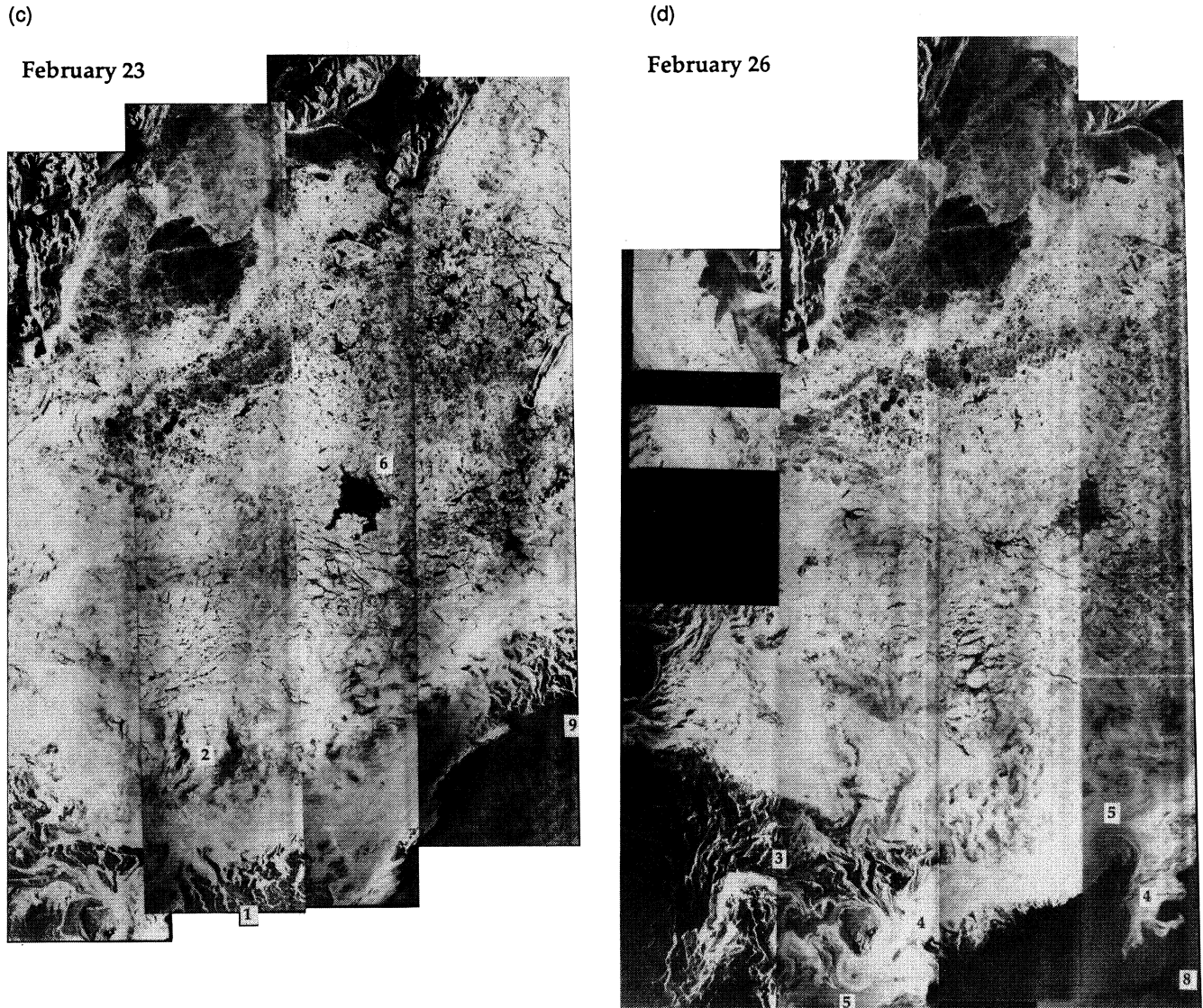
(c)

February 23

(d)

February 26

Fig. 13-13. SAR mosaics obtained during SIZEX'89 on (a) February 17, (b) February 20, (c) February 23, and (d) February 26. (Continued)

essentially like polynyas, are important elements in determining the heat flux from the ocean to the atmosphere in this region, and they demonstrate the usefulness of SAR observations for climate studies on regional and global scales.

Another characteristic feature of all the mosaics is a tongue of ice projecting out of the ice edge, with a typical scale in the range of 20 to 40 km, which is located in the mosaics by the number 4. A tongue of ice is advected southwards on the eastern side of Bjørnøya, and is present in all four mosaics, especially in Figures 13-13(c) and (d); a second tongue is located approximately 100 km east of Bjørnøya. On February 17, observations from the ship showed that this tongue was made up of pancake ice. Three days later the tongue was less pronounced, but in the images it becomes clearly defined. The ice tongues are

associated with a southerly extent of cold water. In many cases they are associated with the occurrence of eddies, located on the mosaics by the number 5. For example, on February 26, two eddies are clearly seen within a tongue. In the second tongue, several eddy features and meanders develop. The time scale of the tongues and eddies is estimated to be a few days. It is possible that the features can propagate, but the data set does not give an indication of a propagation speed.

Polynyas are also conspicuous in these mosaics and are located by the number 6. The 50-km polynya, which was observed in the mosaics of February 23 and 26 west of Hopen, changed its shape as it moved westwards. Greater ice speed on its northern side compared to its southern side caused a stretching and rotation of the polynya as it propagated westward. For the three-day period between the SAR

images, the polynya propagated westward at 10 to 20 km per day. The thin ice within the polynya, which can clearly be seen from the fracture patterns in the images, appears to grow thicker during this three-day interval, as indicated by an increase in the radar backscatter. These images show how useful sequential SAR observations can be in observing and quantifying the growth of thin ice.

The Barents Sea ice cover is exposed to frequent and large swell penetration generated by storms in the North Atlantic and the Norwegian Sea. These swells propagate deep into the ice pack and are a major mechanism for fracturing floes, resulting in the small floe size west of Hopen. An example of this swell penetration is seen in the SAR image acquired on February 23 (Figure 13-14). The swell patterns in the ice cover are clearly visible throughout the entire image. These observations and two-dimensional fast Fourier transform (FFT) analysis indicate that the typical wavelength is 200 m. The swell propagates in a northeasterly direction and the waves refract around Bjørnøya. Another important mechanism for the production of small ice floes in this region is the fracturing of large floes by icebergs, as shown in Figure 13-1(d) [Johannessen et al., 1991b]. These combined mechanisms produce the small floe-size distribution in the Barents Sea west of Hopen. East of Hopen, where the ice floes consistently have large sizes, on the order of tens of kilometers, this combined effect is absent.

13.3 MODELING SEASONAL ICE ZONE PROCESSES

The series of experiments discussed above has demonstrated that the processes in the seasonal ice zone are complicated and not fully understood. The results of these experiments have provided quantitative information on which to base new models. The NORSEX results that showed upwelling along the ice edge prompted Røed and O'Brien [1983] to simulate this process with a coupled nonlinear model. This model included internal ice stress, had a variable ice concentration, and was forced by wind stresses on the ice and ocean. The model demonstrated that winds blowing along the ice edge and to the left when facing the ice cause upwelling along the ice edge. The same model was used by Smedstad and Røed [1985] to study ice edge breakup and banding. These studies emphasized the sensitivity of the response of the coupled system to wind direction and drag coefficients. Häkkinen [1986a, b] extended Røed and O'Brien's work by including nonlinear ocean dynamics. The width of the upwelling zone is determined by the baroclinic Rossby radius of deformation. The jet associated with upwelling is more stable than the one generated in a downwelling situation.

The field programs have also shown that mesoscale eddies are an important feature and dynamical component of the SIZ, e.g., Figures 13-1, 13-3, 13-4, and 13-7. This prompted many investigators to model eddy generation, evolution, and decay. Häkkinen [1986b] showed that a spatial variation in the ice cover together with uniform wind forcing can lead to pycnoclinic changes similar to those generated by a small travelling storm system. Shedding of eddies from the ice edge, with the dominance of cyclonic eddies towards the open ocean, and dissipation of anticyclones underneath the ice cover was also demonstrated in this study.

Smith et al. [1984] studied topographic eddy generation near the Molloy Deep in the Fram Strait using a two-layer primitive equation model for the ocean coupled to a free drift ice model. Häkkinen [1987] used a similar, but linearized, ice–ocean model in a study with a smooth shelf break ridge or canyon. For low wind situations, the bottom topography generates both trapped and travelling ice edge features, which do not always correspond directly to oceanic mesoscale features below. Winds that generate downwelling enhance ice edge meanders, while the ice edge stays compact during upwelling conditions, even in the case when a strong baroclinic vortex is developed underneath the ice. The vortices generated in this modeling study always had strong vertical shear. The combined presence of an ice cover and topographical features were thus shown to be a possible cause of baroclinic instability with subsequent mesoscale variability in the ocean. Smith et al. [1988] performed a systematic parameter study to determine the relative importance of various terms in the ice momentum equation for ice adjustment to evolving eddy–jet interaction. An interesting result from this model is that when the wind blows along the ice edge with the ice on the right, anticyclonic eddies rapidly dissipate. This agrees with the field observations from MIZEX'84 when northerly winds dominated and 12 out of 14 observed eddies were cyclonic [Johannessen, J. A., et al., 1987]. Smith and Bird [1991] continued this study by simulating the interaction of an ocean eddy with an ice edge jet. There are many other modeling studies of SIZ processes, including Ikeda [1986, 1989] who developed models for the Labrador Shelf SIZ, and Kantha and Mellor [1989] who included tides and thermodynamics in a model of the Bering Shelf SIZ.

The field investigations showed that ice bands are a common feature in the SIZ, e.g., Figures 13-7, 13-10, and 13-13. As a result, they have been modeled by many investigators. Wadhams [1983] used wave radiation pressure to generate bands parallel to the ice edge, under off-ice wind conditions. Muench et al. [1983] proposed a model where internal waves generated surface divergence and convergence zones that resulted in ice band formation. In the ice breakup and ice band model by Smedstad and Røed [1985], the formation of ice bands takes approximately 12 days because the ice breakup depends on the development of strong, along ice-edge velocities in the ocean. Chu [1987a] used thermally generated surface winds blowing from ice to water (ice breeze) to force the drift of ice floes. Ice bands resulted from changes in the surface temperature gradients. Another model takes into account the effects of the ocean, so the three media are linked through the surface temperature gradient and the interfacial stresses [Chu, 1987b]. All of these band models use different physics but
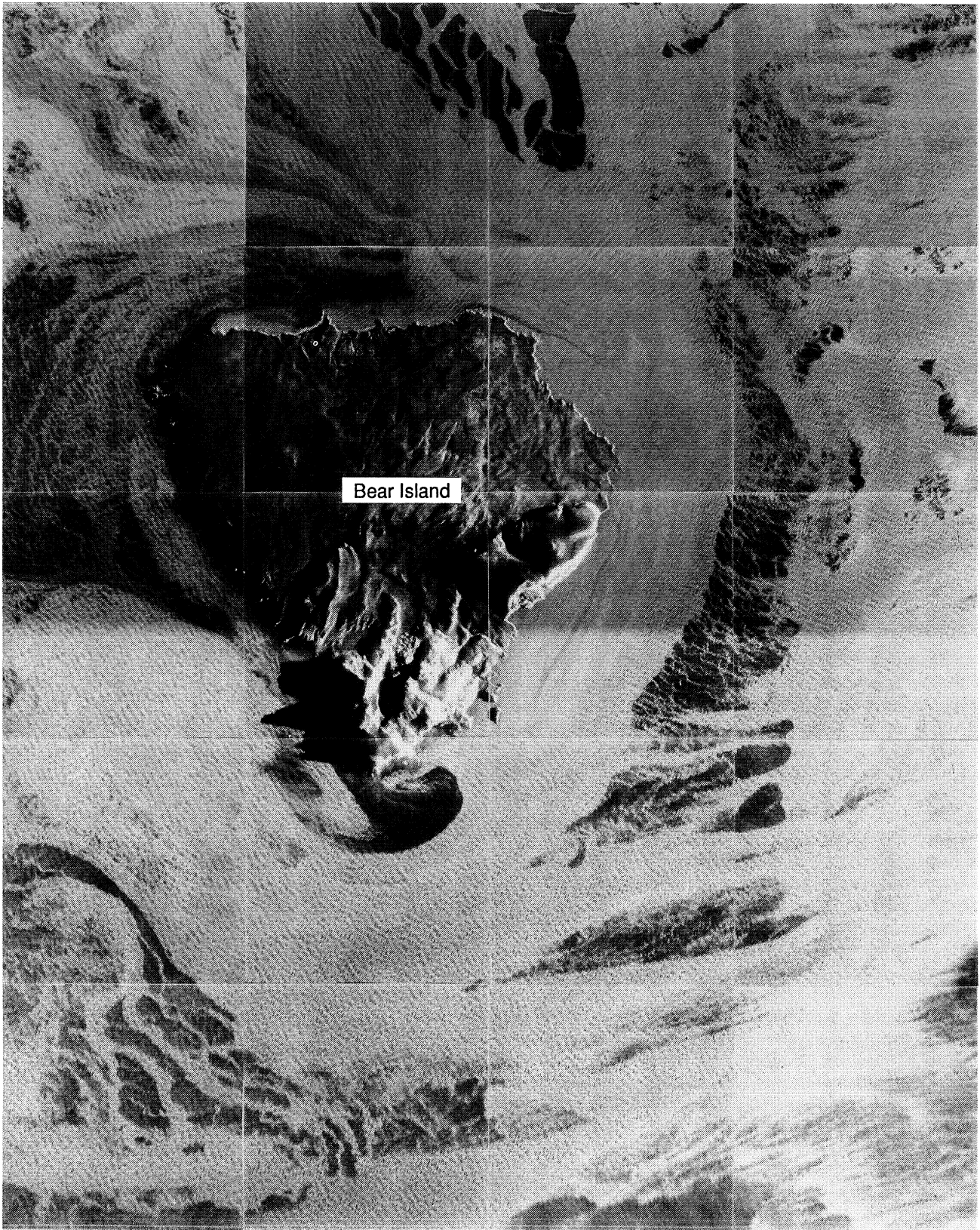
Fig. 13-14. SAR image of the Bjørnøya area obtained on February 23, 1989, illustrating swell propagation in a northeasterly direction around Bjørnøya.

generate similar results, which indicates the need for more detailed observations and model development.

Leads and polynyas have previously been treated in large-scale studies of the interior Arctic [Campbell et al., 1984] and in the Antarctic [Zwally et al., 1983]. The SIZ field experiments have shown that leads and polynyas are also a common mesoscale phenomena, e.g., Figures 13-7 and 13-13. Lead and polynya formation results from the complex interaction of many of the processes that occur in the SIZ. Smedstad and Røed [1985] have proposed a model that simulates ice divergence in the ice-edge region. Ikeda [1985, 1991] has developed wind-driven models for ice motion, including the generation of shore leads and eddy-like features. However, no existing model adequately explains the formation of leads and polynyas within the seasonal ice zone.

The results from the SIZ experiments show that the structure of the seasonal ice zone is fundamentally different from that of the interior ice packs. Compared to the interior ice pack, the SIZ ice pack contains relatively more new ice types and smaller ice floes, is subject to stronger divergence and convergence, undergoes wave penetration, and receives greater snowfall. All presently known SIZ models rely on the continuum hypothesis, which states that all state variables (ice velocity, thickness, etc.) should be continuous functions of position on scales down to the model resolution, e.g., Hibler [1979]. This criteria is not satisfied for SIZ models with resolutions on the order 1 km because of the large variations in floe sizes found in the East Greenland and Barents Seas, as shown in Figures 13-7 and 13-10. None of the models that have been described take specific account of floe size distribution nor try to predict it. However, in an idealized collisional rheology [Shen et al., 1987], the internal ice stresses depend quadratically on the floe size.

Based on the SAR images obtained during the campaigns since 1979, a conceptual SAR model for the seasonal ice zone has been formulated to identify the different ice edge processes (Table 13-3). In this scheme, the ice edge configurations from SAR images have been classified and related to atmospheric and ocean conditions [Johannessen, J. A., et al., 1991]. This conceptual SAR model provides useful guidelines for further numerical modeling of the seasonal ice zone. A realistic ice model should be coupled to the ocean both dynamically and thermodynamically. Thereby the ice can be influenced by ocean currents and waves and melting/freezing can take place. Internal ice stress should be parameterized in a way that is relevant for the SIZ. The wind forcing should act on both ice and ocean, using drag coefficients that depend on ice roughness and concentration. It is not practical to include all these effects in a model at the same time. A useful approach is to divide the overall modeling problem into subproblems that are studied separately and can be verified by SAR observations. Such subproblems could include: developing an ice rheology based on variations in floe size, ice concentration, ice type, ice motion, ridging and rafting, and wave penetration;

determining the temporal and spatial aspects of the ice edge variability; observing melting and freezing events and using them to develop a realistic thermodynamic model; and improving modeling of ice bands.

13.4 Regional forecasting using microwave observations

The Barents Sea is an important region for fisheries, as well as oil exploration. Ice forecasting is therefore a needed service for these industries. The Hibler–Preller ice model for the Barents Sea has been implemented at the Nansen Center for operational use in the Norwegian Ocean Monitoring and Forecasting System with a spatial resolution of 20 km [Hibler, 1979; Preller et al., 1989; Skagseth et al., 1991]. The model is initialized using ice concentration estimates from SSM/I data transferred from the Civilian Navy Ocean Data Distribution System in Monterey, California, to the Nansen Center in near-real time. The model predicts ice motion and concentration for 2 to 5 days with wind forecasts as the driving force. The 24- and 48-hour forecast of ice concentration is compared with updated SSM/I observations. Every 48 hours, the model is restarted with updated ice concentration data from SSM/I. An example of the ice forecast is shown in Figure 13-15. This forecasting scheme represents a considerable improvement compared to running the model without SSM/I data. With a 20-km resolution, the model is not capable of resolving
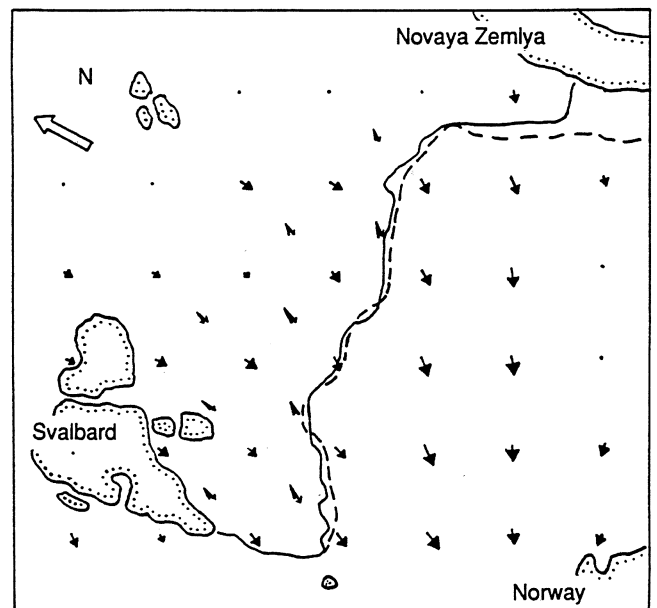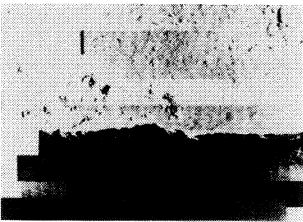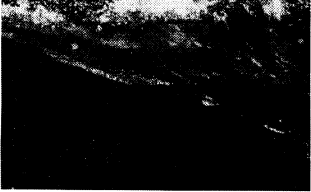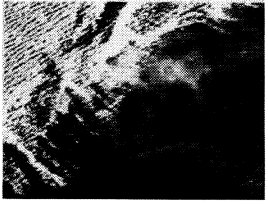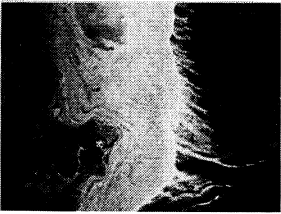

Fig. 13-15. Ice forecasting model for the Barents Sea using real-time ice concentration from SSM/I. The fully drawn line is the observed ice edge, represented by the 30% isoline for ice concentration. The dashed line is the 24-hour forecast for this line. The 24-hour wind forecast is indicated by arrows. The predicted ice motion is 10° to 20° to the right of the wind vectors (indicated by some V-shaped twin vectors inside the ice edge).

TABLE 13-3. Conceptual SAR model for the seasonal ice zone.

SAR Image Example	SAR Ice Edge Configuration	Ice Edge Process	Atmospheric Conditions	Upper Ocean Conditions
	Straight	Upwelling	Parallel Strong to Moderate Wind	Along Ice Jet and Divergent Ekman Flow and Convection
	Meandering and Eddies	Ice-Ocean Eddies	Moderate to Calm Wind	Ocean Eddies, Precondition, Convection
	Ice Jet Perpendicular to the Edge	Momentum Pulse, Ice Jet, and Vortex-Pair	Moderate to Calm Wind	Shallow Upper-Layer Ocean Jet
	Low Backscatter off the Ice Edge and in Leads	Ice Freezing (Winter) / Ice Melting (Summer)	Calm or Off-Ice Wind / Sun Radiation	Salinity and Density Increase, Convection / Fresh Water, Increased Stratification
	Wave Pattern and Compact Small Floes	Wave Propagation, Refraction, and Attenuation	On-Ice Wind	Wind Waves and Swell Propagating Towards the Ice
	Ice Banding, Streamers, and Internal Waves	Ice Bands and Internal Waves	Off-Ice Wind or Varying Wind	Convergence, Divergence, Internal Waves

mesoscale processes, however rapid changes of ice edge position due to wind forcing or freezing/melting is simulated reasonably well by the model. The microwave observations have proven to be indispensable in operational monitoring and forecasting on a regional scale. At present, SAR data from ERS-1 is implemented in the ice monitoring scheme at the Nansen Center and will also be assimilated into mesoscale models.

13.5 THE SIZ IN THE CLIMATE SYSTEM

Sea ice is an important part of the global climate system. The two key aspects of the complex and dynamic sea ice covers are ice extents and the area of open water within the ice. The sea ice extent affects the amount of solar radiation absorbed in its hemisphere and alters the atmosphere–ocean exchanges of heat, moisture, and momentum. Ice-free oceans generally have an albedo of 10 to 15% [Lamb, 1982], whereas sea ice albedos average about 80% [Washington and Parkinson, 1986]. Because of this great contrast between ice and ocean albedos, the presence of sea ice considerably reduces the amount of solar radiation observed at the Earth's surface. Since sea ice covers such a large area of the Earth's surface, a number of investigators have studied the variations of the ice extent of the polar regions for evidence of climate change. They have examined the existing satellite record of ice extents of both the Antarctic sea ice cover [Zwally et al., 1983] and the Arctic sea ice cover [Campbell et al., 1984; Parkinson et al., 1987; Gloersen and Campbell, 1988; Parkinson and Cavalieri, 1989]. The sea ice extent extrema were first studied on a global scale by Gloersen and Campbell [1988] for both ESMR and SMMR. Recently, Gloersen and Campbell [1991a, b] have extended the SMMR analysis using the corrected data set.

While the ice extent is determined by SIZ processes, open water occurs in varying amounts throughout the whole ice cover [Campbell et al., 1984; Parkinson et al., 1987]. The area of open water within the ice pack, small even compared with the ice extent, is critically important because the fluxes of heat and moisture through a given area of open water are 2 to 3 orders of magnitude greater than through the same area of sea ice [Maykut, 1978]. The multispectral and dual-polarized observations with the SMMR allow determinations of ice extent and open water with greater accuracies than those obtainable with earlier satellite sensors [Gloersen and Campbell, 1991a].

In this section, we present the SMMR results for ice extent and open water amounts and variations for the Arctic and Antarctic ice covers and for the Greenland and Barents–Kara Seas. Gloersen and Campbell [1991b] used a band-limited regression technique [Lindberg, 1991] to obtain ice extent trends of the Arctic and Antarctic ice covers for the almost nine-year-long SMMR record. The time series of the SMMR records for each hemisphere and their trends are shown in Figure 13-16. These data show that the trends of the polar ice extents were not in phase:
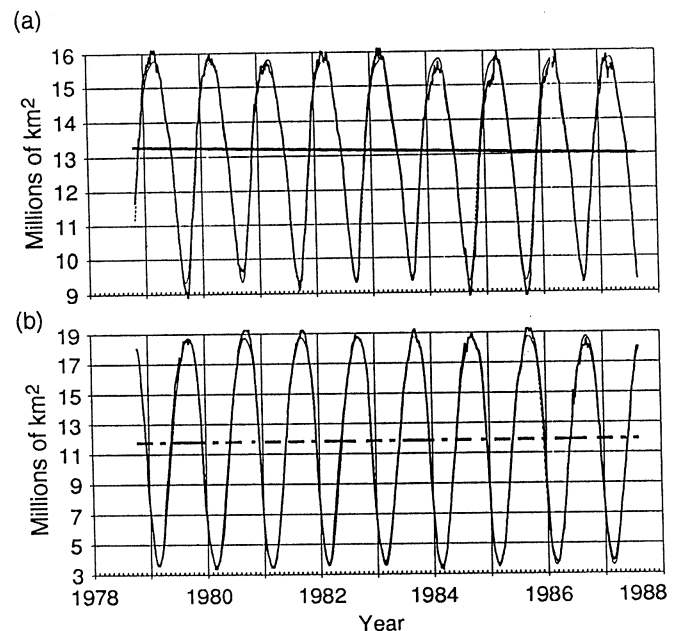

Fig. 13-16. Time series of ice extent derived from SMMR data from the (a) Arctic and (b) Antarctic [Gloersen and Campbell, 1991b]. The solid line for the Arctic ice extent shows the statistically significant decline of approximately 2%. The dashed line for the Antarctic ice extent indicates no statistically significant trend.

The Arctic had a statistically significant negative trend of ~2%, whereas the Antarctic had no significant trends.

The Greenland Sea SMMR records of ice extent, annually averaged ice extent and trends, and open water amount are shown in Figure 13-17 [Gloersen et al., 1992]. There are a number of noteworthy features in the oscillatory record of the sea ice in these figures. The amplitude of the annual cycle varies by an average of 50% during the nine-year period, with the smallest peak in ice extent occurring in 1984, the only year in which the Odden was absent. The area of open water is 2 to 4×10^5 km^2, about one-third of the ice-covered area. There is generally more open water during the winter than in the summer because the winter ice extent is greater and the pack undergoes divergence due to winter storms. Significantly large amounts of open water occur during all seasons. The SMMR record of the annually averaged ice extent in the Greenland Sea shows a negative trend of ~4%.

The SMMR records for the Barents and Kara Seas are shown in Figure 13-18 [Gloersen et al., 1992]. In this combined region, the ice extent undergoes even larger annual variations than in the Greenland Sea, expanding from about 0.7×10^6 km^2 in September to about 1.9×10^6 km^2 in April. Similar to the Greenland Sea, the Kara and Barents Seas region exhibits strong interannual difference in both the summer and the winter months [Gloersen et al., 1992]. The SMMR record of the annually averaged ice extent for the Barents and Kara Seas reveals a large negative trend of ~14%. The SMMR record of open water
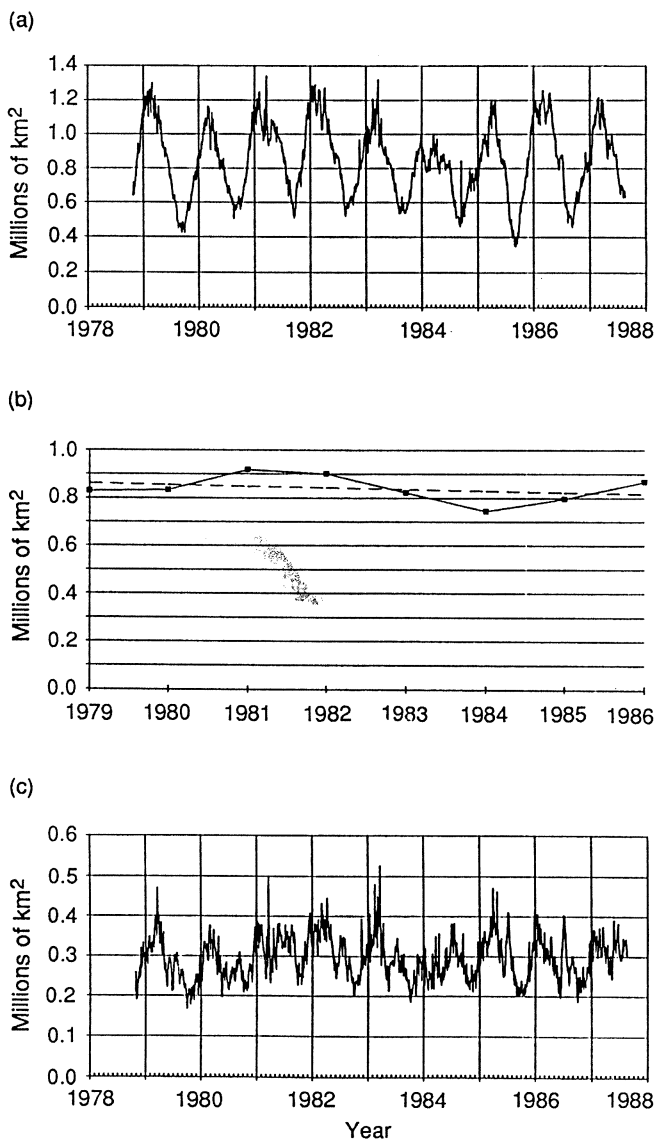
(a)

(b)

(c)

Fig. 13-17. (a) Time series of SMMR data from the Greenland Sea ice extent, (b) annually averaged sea ice extent, and (c) open water within the ice pack [Gloersen and Campbell, 1991a].
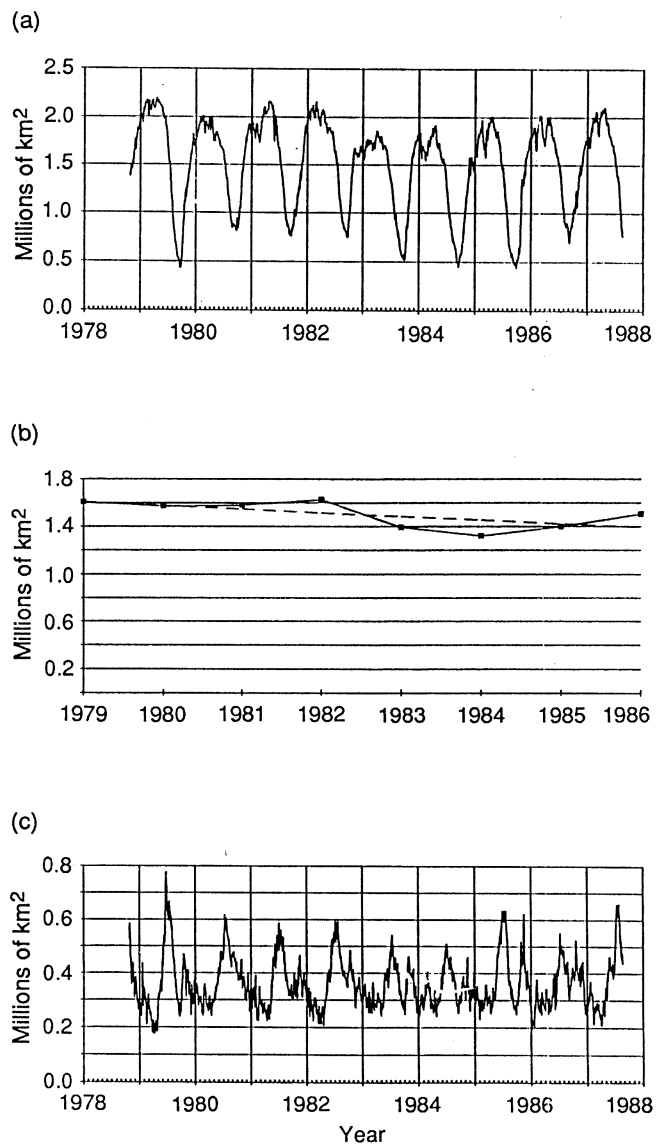
(a)

(b)

(c)

Fig. 13-18. (a) Time series of SMMR data from the Barents and Kara Sea ice extent, (b) annually averaged sea ice extent, and (c) open water within the ice pack [Gloersen and Campbell, 1991a].

amounts in the Barents and Kara Seas shows that generally more open water occurs in the summer than in the winter.

During the SMMR years, the negative trend of the annually average ice extents that occurred in the Greenland, Barents, and Kara Seas occurred in only one other Arctic Sea, the Sea of Okhotsk. Positive trends occurred in the Arctic Ocean, Bering Sea, Hudson Bay, Baffin Bay, Daris Strait, and Labrador Sea. But the combined effect of these positive trends was not sufficient to cancel out the negative trends of the other seas [Gloersen et al., 1992]. Therefore, the negative trends of the Greenland, Barents, and Kara Seas played a dominant role in determining the overall

negative trend in ice extent of 2% for the entire Arctic during the SMMR period.

The dominant retreat of sea ice in the passive microwave data record occurs in the region of the Atlantic approach to the Arctic Ocean. Many different mechanisms may contribute to such variations. It may be part of a self-sustained interdecadal cycle involving changes in the atmospheric circulation, surface freshwater flux, and deep water formation [Dickson et al., 1988; Mysak et al., 1990; Ikeda, 1990; Johannessen et al., 1991a]. Subtle changes in the complicated mesoscale processes discussed in the previous section may contribute to this kind of variability.

Recent results from global ocean–atmosphere climate models [Stouffer et al., 1989; Manabe et al., 1990, 1991a, b; Cubasch et al., 1991] show a large sensitivity of the present climate in this region to increased greenhouse gas forcing, as previously indicated in the ice–ocean model by Semtner [1987] and discussed by a large number of authors. Numerical models that both resolve the in- and outflows to the North Atlantic [Oberhuber, 1990] and include proper sea ice dynamics are needed to investigate whether these sensitivities are realistic.

The present time series of passive microwave observations from satellites is obviously too short to distinguish between natural variability and anthropogenic change. It is also too short to make any definitive statement of a climate trend. However, the quality of the data offers unprecedented possibilities for model testing. Figure 13-19 shows ice concentrations in the Northern Hemisphere from an ice–ocean model [Oberhuber, 1990] and SSM/I observations for the month of February. More detailed model–data comparisons should at least allow a proper assessment of the quality of present large-scale models.

Continuous, accurate monitoring of sea ice variations from passive microwave instruments will be able to determine future fingerprints of an anticipated global warming. Use of these data in large-scale numerical models, which include parameterizations of the smaller scale processes discussed previously, will be crucial to achieving a better understanding of the role of regional climate processes in the global system. Both active and passive microwave data can therefore be expected to play a major role in climate research in the future.

REFERENCES

Burns, B. A., D. J. Cavalieri, M. R. Keller, W. J. Campbell, T. C. Grenfell, G. A. Maycut, and P. Gloersen, Multisensor comparison of ice concentration estimates in the marginal ice zone, *Journal of Geophysical Research, 92(C7)*, pp. 6843–6856, 1987.

Campbell, W. J., J. Wayenberg, R. O. Ramseier, M. R. Vant, R. Weaver, A. Redmond, L. Arsenault, P. Gloersen, H. J. Zwally, T. T. Wilheit, T. C. Chang, D. Hall, L. Gray, D. C. Meeks, M. L. Bryan, F. T. Barath, C. Elachi, F. Leberl, and T. Fan, Microwave remote sensing of sea ice in the AIDJEX main experiment, *Boundary Layer Meteorology, 13*, pp. 309–337, 1978.
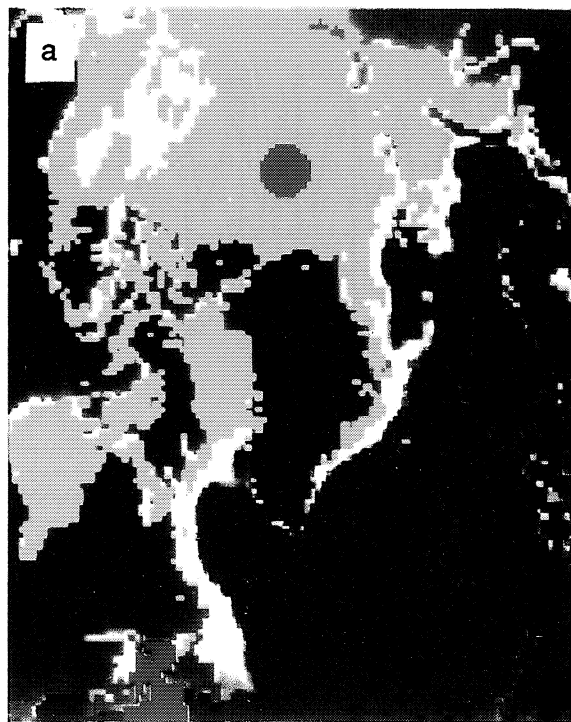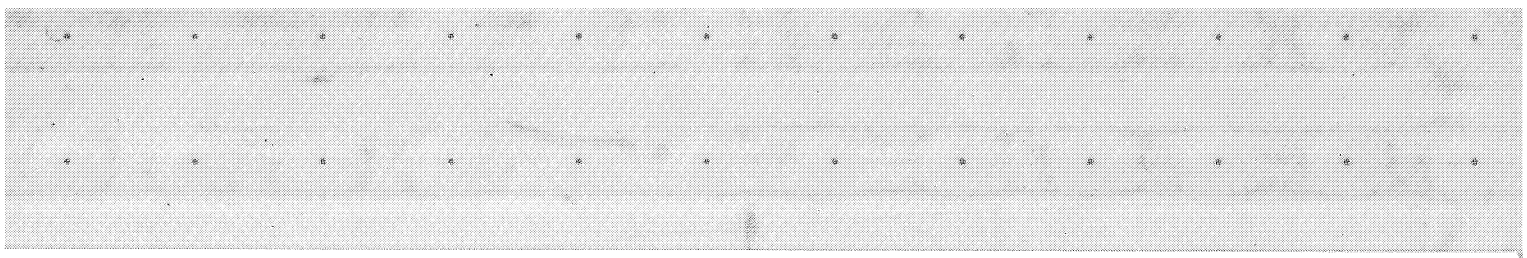

Fig. 13-19. (a) Sea ice concentration for February 1989, in the Northern Hemisphere as observed by SSM/I (yellow: >90% and blue: <10%); and (b) simulated ice concentrations for a typical February from the model by Oberhuber [1990] (red: >90% and dark blue: <10%).

Campbell, W. J., P. Gloersen, and H. J. Zwally, Aspects of Arctic sea ice observable by sequential passive microwave observations from the Nimbus-5 satellite, *Arctic Technology and Policy*, edited by I. Dyer and C. Chryssostomidis, pp. 197–222, Hemisphere Publishing Corporation, New York, 1984.

Campbell, W. J., P. Gloersen, E. G. Josberger, O. M. Johannessen, P. S. Guest, N. Mognard, R. Shuchman, B. A. Burns, N. Lannelongue, and K. Davidson, Variation of mesoscale and large-scale ice morphology in the 1984 Marginal Ice Zone Experiment as observed by microwave remote sensing, *Journal of Geophysical Research, 92(C7)*, pp. 6805–6824, 1987.

Chu, P. C., An ice breeze mechanism for an ice divergence-convergence criterion in the Marginal Ice Zone, *Journal of Physical Oceanography, 17(10)*, pp. 1627–1632, 1987a.

Chu, P. C., An instability theory of ice–air interaction for the formation of ice edge bands, *Journal of Geophysical Research, 92*, pp. 6966–6970, 1987b.

Coon, M. D., A review of AIDJEX modeling, *Sea Ice Processes and Models, Proceedings of the Arctic Ice Dynamics Joint Experiment International Commission on Snow and Ice Symposium*, University of Washington Press, 474 pp., 1980.

Cubasch, U., K. Hasselmann, H. Höck, E. Maier–Reimer, U. Mikolajewicz, B. D. Santer, and R. Sausen, *Time-Dependent Greenhouse Warming Computations With a Coupled Ocean–Atmosphere Model*, Report 67, 18 pp., Max-Planck-Institute für Meteorologie, Hamburg, Germany, 1991.

Dickson, R. R., J. Meincke, S.–A. Malmberg, and A. J. Lee, The great salinity anomaly in the Northern North Atlantic 1968–1982, *Programmetric Oceanography, 20*, pp. 103–151, 1988.

Fedorov, K. N. and A. I. Ginsburg, Mushroom-like currents (vortex dipoles) in the ocean and in a laboratory tank, *Annals of Geophysics, 4*, p. 507, 1986.

Gloersen, P. and W. J. Campbell, Variations in the Arctic, Antarctic, and global sea ice covers during 1978–1987 as observed with the Nimbus 7 Scanning Multichannel Microwave Radiometer, *Journal of Geophysical Research, 93*, pp. 10,666–10,674, 1988.

Gloersen, P. and W. J. Campbell, Variations of extent, area, and open water of the polar sea ice covers: 1978–1987, *International Conference on the Role of the Polar Oceans in Global Change*, Fairbanks, Alaska, 18 pp., 1991a.

Gloersen, P. and W. J. Campbell, Recent variations in Arctic and Antarctic sea-ice covers, *Nature, 352*, pp. 33–36, 1991b.

Gloersen, P., H. J. Zwally, A. T. C. Chang, D. K. Hall, W. J. Campbell, and R. O. Ramseier, Time dependence and distribution of sea ice concentration and multiyear ice fraction in the Arctic Basin, *Boundary Layer Meteorology, 13(1–4)*, pp. 339–360, 1978.

Gloersen, P., W. J. Campbell, D. J. Cavalieri, J. C. Comiso, C. L. Parkinson, and H. J. Zwally, *Arctic and Antarctic Sea Ice 1978–1987: Satellite Passive Microwave Observations and Analysis*, NASA SP-511, 200 pp., National Aeronautics and Space Administration, Washington, DC, 1992.

Guest, P. S. and K. L. Davidson, The effect of observed ice conditions on the drag coefficient in the summer East Greenland Sea marginal ice zone, *Journal of Geophysical Research, 92*, pp. 6943–6954, 1987.

Häkkinen, S., Coupled ice–ocean dynamics in the marginal ice zones: Upwelling/downwelling and eddy generation, *Journal of Geophysical Research, 91(C1)*, pp. 819–832, 1986a.

Häkkinen, S., Ice banding as a response of coupled ice–ocean systems to temporally varying wind, *Journal of Geophysical Research, 91*, pp. 5047–5053, 1986b.

Häkkinen, S., Feedback between ice flows, barotropic flow, and baroclinic flow in the presence of bottom topography, *Journal of Geophysical Research, 92*, pp. 3807–3820, 1987.

Hibler, W. D, III, A dynamic thermodynamic sea ice model, *Journal of Physical Oceanography, 9*, pp. 815–846, 1979.

Ikeda, M., A coupled ice–ocean model of a wind-driven coastal flow, *Journal of Geophysical Research, 90*, pp. 9119–9128, 1985.

Ikeda, M., A mixed layer beneath melting sea ice in the marginal ice zone using a one-dimensional turbulent closure model, *Journal of Geophysical Research, 91*, pp. 5054–5060, 1986.

Ikeda, M., A coupled ice–ocean mixed-layer model of the Marginal Ice Zone responding to wind forcing, *Journal of Geophysical Research, 94(C7)*, pp. 9699–9709, 1989.

Ikeda, M., Decadal oscillations of the air–ice–ocean system in the Northern Hemisphere, *Atmosphere–Ocean, 28(1)*, pp. 106–139, 1990.

Ikeda, M., Wind-induced mesoscale features in a coupled ice–ocean system, *Journal of Geophysical Research, 96*, pp. 4623–4629, 1991.

Johannessen, J. A., O. M. Johannessen, E. Svendsen, R. Shuchman, T. Manley, W. J. Campbell, E. G. Josberger, S. Sandven, J. C. Gascard, T. Olaussen, K. Davidson, and J. Van Leer, Mesoscale eddies in the Fram Strait Marginal Ice Zone during the 1983 and 1984 Marginal Ice Zone Experiments, *Journal of Geophysical Research, 92*, pp. 6754–6772, 1987.

Johannessen, J. A., E. Svendsen, S. Sandven, O. M. Johannessen, and K. Lygre, Three-dimensional structure of mesoscale eddies in the Norwegian Coastal Current, *Journal of Physical Oceanography, 19*, pp. 3–19, 1989.

Johannessen, J. A., O. M. Johannessen, S. Sandven, and P. M. Haugen, A characterization of air–ice–ocean interactive processes in the MIZ based on SAR-derived ice edge configurations, *IGARSS'91 Proceedings*, pp. 429–432, European Space Agency, Helsinki, Finland, 1991.

Johannessen, O. M., Brief overview of the physical oceanography, *The Nordic Seas*, edited by B. G. Hurdle, pp. 103–127, Springer Verlag, 1986a.

Johannessen, O. M., *Seasonal Ice Zone Experiment, ERS-1 Pre- and Postlaunch Experiments in the Barents Sea, Fram Strait, and Greenland Sea*, NERSC Special Report 18, Nansen Environmental and Remote Sensing Center, Bergen, Norway, 1986b.

Johannessen, O. M., Introduction: Summer Marginal Ice Zone Experiments during 1983 and 1984 in the Fram Strait and the Greenland Sea, *Journal of Geophysical Research, 92*, pp. 6716–6717, 1987.

Johannessen, O. M. and L. A. Foster, A note on the topographically controlled oceanic polar front in the Barents Sea, *Journal of Geophysical Research, 83*, pp. 45–67, 1978.

Johannessen, O. M., J. A. Johannessen, J. H. Morison, B. A. Farrelly, and E. A. S. Svendsen, Oceanographic conditions in the marginal ice zone north of Svalbard in early fall 1979 with emphasis on mesoscale processes, *Journal of Geophysical Research, 88*, pp. 2755–2769, 1983a.

Johannessen, O. M., W. D. Hibler III, P. Wadhams, W. J. Campbell, K. Hasselmann, I. Dyer, and M. Dunbar, *A Science Plan for a Summer Marginal Ice Zone Experiment in the Fram Strait / Greenland Sea*, CRREL Report 83-12, 47 pp., Cold Regions Research and Engineering Laboratory, Hanover, New Hampshire, 1983b.

Johannessen, O. M., W. D. Hibler III, P. Wadhams, W. J. Campbell, K. Hasselmann, and I. Dyer, Marginal ice zones: A description of air–ice–ocean interactive processes, models, and planned experiments, *Arctic Technology and Policy*, edited by I. Dyer and C. Chryssostomidis, pp. 133–146, Hemisphere Publishing Corporation, New York, 1984a.

Johannessen, O. M., J. A. Johannessen, B. Farrelly, K. Kloster, and R. A. Shuchman, Eddy studies during MIZEX'83 by ship and remote sensing observations, *Proceedings of the 1984 IGARSS*, pp. 365–368, ESA SP-215, European Space Agency, Helsinki, Finland, 1984b.

Johannessen, O. M., J. A. Johannessen, E. Svendsen, R. A. Shuchman, W. J. Campbell, and E. G. Josberger, Ice edge eddies in the Fram Strait marginal ice zone, *Science, 236*, p. 427, 1987.

Johannessen, O. M., S. Sandven, and J. A. Johannessen, Eddy-related winter convection in the Boreas Basin, *Deep Convection and Deep Water Formation*, edited by P. C. Chu and J. C. Gascard, pp. 87–105, Elsevier Science Publishers, New York, 1991a.

Johannessen, O. M., S. Sandven, and K. Kloster, Icebergs in the Barents Sea during SIZEX'89, *Proceedings of the Eleventh International Conference on Port and Ocean Engineering Under Arctic Conditions (POAC'91)*, Memorial University of Newfoundland, St. John's, Newfoundland, Canada, 1991b.

Kantha, L. H. and G. L. Mellor, Application of a two-dimensional coupled ocean–ice model to the Bering Sea marginal ice zone, *Journal of Geophysical Research, 94*, pp. 10,921–10,935, 1989.

Lamb, H. H., The climatic environment of the Arctic Ocean, *The Arctic Ocean. The Hydrographic Environment and the Fate of Pollutants*, edited by L. Rey, pp. 135–162, Comite Arctique International, London, 1982.

Leppäranta, M. and W. D. Hibler III, Mesoscale sea ice deformation in the East Greenland Marginal Ice Zone, *Journal of Geophysical Research, 92(C7)*, pp. 7060–7070, 1987.

Lindberg, C. R., Band-limited regression, Part I: Simple linear models. *Journal of the Royal Statistical Society*, Part B, in press, 1991.

Manabe, S., K. Bryan, and M. J. Spelman, Transient response of a global ocean–atmosphere model to a doubling of atmospheric carbon dioxide, *Journal of Physical Oceanography, 20*, pp. 722–749, 1990.

Manabe, S., R. J. Stouffer, M. J. Spelman, and K. Bryan, Transient responses of a coupled ocean–atmosphere model to gradual changes of atmospheric CO_2, Part I: Annual mean response, *Journal of the Climate, 4*, pp. 785–818, 1991a.

Manabe, S., R. J. Stouffer, K. Bryan, and M. J. Spelman, The transient response of the Arctic climate to gradual changes of atmospheric carbon dioxide, AGU Fall Meeting December 9–13, *Supplement to EOS Transactions of AGU*, 1991b.

Maykut, G. A., Energy exchange over young sea ice in the central Arctic, *Journal of Geophysical Research, 83*, pp. 3646–3658, 1978.

MIZEX Group, MIZEX East 83/84: The summer Marginal Ice Zone Program in the Fram Strait/Greenland Sea, *EOS, 67(23)*, pp. 513–517, 1986.

MIZEX Group, MIZEX East 1987: The winter Marginal Ice Zone Program in the Fram Strait/Greenland Sea, *EOS, 70(17)*, pp. 545–555, 1989.

Muench, R., Mesoscale phenomena in the Polar Oceans, *Polar Oceanography*, edited by W. O. Smith, Jr., pp. 223–286, Academic Press, Inc., 1990.

Muench, R. D., P. H. LeBlond, and L. E. Hachmeister, On some possible interactions between internal waves and sea ice in the marginal ice zone, *Journal of Geophysical Research, 88(C5)*, pp. 2819–2826, 1983.

Mysak, L. A., D. K. Manak, and R. F. Marsden, Sea-ice anomalies observed in the Greenland and Labrador Seas during 1901–1984 and their relation to an interdecadal Arctic climate cycle, *Climate Dynamics, 5*, pp. 111–133, 1990.

NORSEX Group, The Norwegian remote sensing experiment in a marginal ice zone, *Science, 220(4599)*, pp. 781–787, 1983.

Oberhuber, J. M., *Simulation of the Atlantic Circulation With a Coupled Sea-Ice–Mixed-Layer Isopycnal General Circulation Model*, Report No. 59, Max-Planck-Institut für Meteorologie, Hamburg, Germany, 1990.

Parkinson, C. L. and D. J. Cavalieri, Arctic sea ice 1973–1987: Seasonal, regional, and interannual variability, *Journal of Geophysical Research, 94*, pp. 14,499–14,523, 1989.

Parkinson, C. L., J. C. Comiso, H. J. Zwally, D. J. Cavalieri, P. Gloersen, and W. J. Campbell, *Arctic Sea Ice, 1973–1976: Satellite Passive-Microwave Observations*, NASA SP-489, 296 pp., National Aeronautics and Space Administration, Washington, DC, 1987.

Preller, R. H., S. Riedlinger, and P. G. Posey, *The Regional Polar Ice Prediction Systems Barents Sea (RPIPS-B): A technical description*, NORDA Report 182, Naval Oceanographic and Atmospheric Research Laboratory, Stennis Space Center, Mississippi, 1989.

Pritchard, R. S., *Sea Ice and Models, Proceedings of the Arctic Ice Dynamics Joint Experiment, International Commission on Snow and Ice Symposium*, University of Washington Press, Seattle, Washington, 474 pp., 1980.

Røed, L P. and J. J. O'Brien, A coupled ice–ocean model of upwelling in the marginal ice zone, *Journal of Geophysical Research, 88*, pp. 2863–2872, 1983.

Sandven, S. and O. M. Johannessen, High-frequency internal wave observations in the marginal ice zone, *Journal of Geophysical Research, 92*, pp. 6911–6920, 1987.

Sandven, S. and O. M. Johannessen. Seasonal ice zone studies, *The Sea. Ocean Engineering Science. Volume 9*, John Wiley and Sons, Inc., pp. 567–592, 1990.

Sandven, S. and O. M. Johannessen, Sea ice studies in the Barents Sea, *Journal of Photogrammetry and Remote Sensing*, in press, 1992.

Sandven, S., O. M. Johannessen, and P. M. Haugan., *A Study of the Marginal Ice Zone, Summary Report*, NERSC Technical Report 61, Nansen Environmental and Remote Sensing Center, Bergen, Norway, 1991a.

Sandven, S., K. Kloster, and O. M. Johannessen, *SAR Ice Algorithms for Ice Edge, Ice Concentration, and Ice Kinematics*, Nansen Environmental and Remote Sensing Center Technical Report 38, Bergen, Norway, 1991b.

Semtner, A. J., Jr., A numerical study of sea ice and ocean circulation in the Arctic, *Journal of Physical Oceanography, 17*, PP. 1077–1099, 1987.

Shen, H. H., W. D. Hibler III, and M. Leppäranta, The role of floe collisions in sea ice rheology, *Journal of Geophysical Research, 92*, pp. 7085–7096, 1987.

Shuchman, R. A., B. A. Burns, O. M. Johannessen, E. G. Josberger, W. J. Campbell, T. O. Manley, and N. Lannelongue, Remote sensing of the Fram Strait Marginal Ice Zone, *Science, 236*, pp. 429–431, 1987.

SIZEX Group, *SIZEX'89, A Prelaunch ERS-1 Experiment*, Nansen Environmental and Remote Sensing Center Technical Report 23, Bergen, Norway, 1989.

Skagseth, Ø., P. M. Haugan, S. Sandven, O. M. Johannessen, K. Kloster, and Å. R. Nilsen, Demonstration of Operational Ice Forecasting in the Barents Sea, Nansen Environmental and Remote Sensing Center Special Report 10, Bergen, Norway, 1991.

Smedstad, O. M. and L. P. Røed, A coupled ice–ocean model of ice break-up and banding in the marginal ice zone, *Journal of Geophysical Research, 90(C1)*, pp. 876–882, 1985.

Smith, D. C., IV, and A. A. Bird, The interaction of an ocean eddy with an ice edge ocean jet in a marginal ice zone, *Journal of Geophysical Research, 96(C3)*, pp. 4675–4690, 1991.

Smith, D. C., IV, J. Morison, J. A. Johannessen, and N. Untersteiner, Topographic generation of an eddy at the edge of the East Greenland Current, *Journal of Geophysical Research, 89*, pp. 8205–8208, 1984.

Smith, D. C., IV, A. A. Bird, and W. P. Budgell, A numerical study of mesoscale ocean eddy interaction with a marginal ice zone, *Journal of Geophysical Research, 93(C10)*, pp. 12,461–12,473, 1988.

Stouffer, R. J., S. Manabe, and K. Bryan, Interhemispheric asymmetry in climate response to a gradual increase of atmospheric CO_2, *Nature, 342*, pp. 660–662, 1989.

Svendsen, E., K. Kloster, B. Farrelly, O. M. Johannessen, J. A. Johannessen, W. J. Campbell, P. Gloersen, D. Cavalieri, and C. Mätzler, Norwegian Remote Sensing Experiment: Evaluation of the Nimbus 7 Scanning Multichannel Microwave Radiometer for sea ice research, *Journal of Geophysical Research, 88(C5)*, pp. 2781–2792, 1983.

Untersteiner, N., *The Geophysics of Sea Ice*, pp. 1–8, Plenum Press, New York, 1986.

Wadhams, P., A mechanism for the formation of ice edge bands, *Journal of Geophysical Research, 88(C5)*, pp. 2813–2818, 1983.

Wadhams, P., The seasonal sea ice zone, *The Geophysics of Sea Ice*, edited by N. Untersteiner, pp. 825–992, Plenum Press, New York, 1986.

Washington, W. M. and C. L. Parkinson, *An Introduction to Three-Dimensional Climate Modeling*, University Science Books, Mill Valley, California, 1986.

Zwally, H. J., J. C. Comiso, C. L. Parkinson, W. J. Campbell, F. D. Carsey, and P. Gloersen, *Antarctic Sea Ice, 1973–1976: Satellite Passive-Microwave Observations*, 206 pp., NASA SP-459, National Aeronautics and Space Administration, Washington, DC, 1983.